Tau accumulation in astrocytes of the dentate gyrus induces neuronal dysfunction and memory deficits in Alzheimer's disease

Kevin Richetin[1,2,3], Pascal Steullet[1], Mathieu Pachoud[2,3], Romain Perbet[4], Enea Parietti[1], Mathischan Maheswaran[2,3], Sabiha Eddarkaoui[4], Séverine Bégard[4], Catherine Pythoud[2,3], Maria Rey[2,3], Raphaëlle Caillierez[4], Kim Q Do[1], Sophie Halliez[4], Paola Bezzi[5] Luc Buée[4], Geneviève Leuba[1], Morvane Colin[4], Nicolas Toni[1*], Nicole Déglon[2,3*]

Author's affiliations

[1] Center for Psychiatric Neuroscience, Department of Psychiatry, Lausanne University Hospital (CHUV) and University of Lausanne, 1008 Prilly-Lausanne, Switzerland;

[2] Lausanne University Hospital (CHUV) and University of Lausanne, Neuroscience Research Center (CRN), Laboratory of Neurotherapies and Neuromodulation, 1011 – Lausanne, Switzerland

[3] Lausanne University Hospital (CHUV) and University of Lausanne, Department of Clinical Neuroscience (DNC), Laboratory of Neurotherapies and Neuromodulation, 1011 – Lausanne, Switzerland

[4] University of Lille, Institut National de la Recherche (INSERM), CHU-Lille, UMR-S 1172, Lille Neuroscience & Cognition, Lille, France.

[5] Department of Fundamental Neurosciences, University of Lausanne, 1005 Lausanne, Switzerland

*Equal contribution

Corresponding authors:

Kevin Richetin: kevin.richetin@chuv.ch

Nicolas Toni: nicolas.toni@unil.ch

Abstract

Alzheimer's disease (AD) is characterized by the accumulation of the tau protein in neurons, neurodegeneration and memory loss. However, the role of non-neuronal cells in this chain of events remains unclear. In the present study, we found accumulation of tau in hilar astrocytes of the dentate gyrus of AD patients. In mice, the overexpression of 3R tau specifically in hilar astrocytes of the dentate gyrus altered mitochondrial dynamics and function. In turn, these changes led to a reduction of adult neurogenesis, parvalbumin-expressing neurons, inhibitory synapses, and hilar gamma oscillations, which were accompanied by impaired spatial memory performances. Together, these results indicate that the loss of tau homeostasis in astrocytes of the hilus of the dentate gyrus is sufficient to induce AD-like symptoms, through the impairment of the neuronal network. These results are important for our understanding of disease mechanisms and underline the crucial role of astrocytes in hippocampal function.

Introduction

Tau is a microtubule-associated protein, abundant in the nervous system, which stabilizes microtubules and promotes their assembly. Alternative splicing produces six tau isoforms that can contain either three (3R) or four (4R) microtubule-binding repeats in the carboxy-terminal half, and between zero and two (0–2N) amino-terminal inserts. They are therefore referred to as: 0N3R; 1N3R; 2N3R; 0N4R; 1N4R and 2N4R[1]. In the healthy adult human brain, the 3R and 4R isoforms of tau are equimolar, but a disruption of the 3R to 4R ratio is sufficient to drive tau aggregation[2] and the production of neurofibrillary tangles in pathological aging[3] and tauopathies[4].

By virtue of its unique plasticity and its integrative properties, the hippocampus plays a fundamental role in memory formation. In Alzheimer's disease (AD) as well as in several tauopathies, the hippocampal formation is largely impacted by the accumulation of hyperphosphorylated tau, accompanied by a reduction in synapse number, decreased adult neurogenesis and neurodegeneration[5]. However, the contribution of non-neuronal cell types, and in particular of astrocytes, to the functional deficiency of the hippocampus is unclear. In physiological conditions, astrocytes contribute to neuronal function and plasticity by several modes of regulation[6]. Thus, alterations in astrocytic function may participate to disease phenotype, but the extent of this participation is currently unclear.

Results

Accumulation of 3R tau in hilar hippocampal astrocytes of AD patients

We examined the density of cells expressing a pathological form of phospho-tau in different regions of the hippocampus AD healthy age- and sex-matched donors (**Supplementary Table and Data Extended Fig. 1 a-c**). We used immunohistochemistry with an AD2 antibody, which recognizes the phosphorylated Ser-396 and Ser-404 epitopes[7] (**Fig. 1a**). We found a strong variability in the density of $AD2^+$ cells between hippocampal structures but also between patients, whereas healthy donors showed no AD2 immunoreactivity (**Fig. 1b**). For each patient, we found that the granule cell layer of the dentate gyrus (GCL), CA1 and CA3 regions exhibited a higher density of $AD2^+$ cells than the hilus and molecular layer (ML) of the dentate gyrus (**Fig. 1b**). However, when patients were staged according to the Braak scale, we found a strong correlation between Braak stage and the density of $AD2^+$ cells in the dentate gyrus (including the ML, GCL and hilus, **Fig. 1c-d**). A great variability in the number of hippocampal amyloid plaques was also observed between patients and stages. However, we found no correlation between Braak stage and hippocampal plaque number (**Data Extended Fig. 1, d-f**). Thus in the hippocampus, the dentate gyrus and in particular the hilus, is increasingly affected by the progression of tau pathology in AD.

We next examined the presence of 3R and 4R tau isoforms in the hilus of healthy donors and AD patients using isoform-specific antibodies (**Data Extended Fig. 2**). The density of 3R tau inclusions in the hilus was higher in AD patients presenting hyperphosphorylated tau and this increase was exacerbated in patients who also exhibited amyloid plaques in the hilus. In contrast, the density of hilar 4R inclusions was only increased in patients devoid of hyperphosphorylated tau or amyloid plaques, suggesting a transient increase along the course of the disease (**Fig. 1e-h).**

AD is considered to be primarily a neuronal disease. However, tau has also been found in astrocytes of AD patients, with much less known consequence[8]. We therefore examined the presence of 3R or 4R tau in astrocytes in the hilus of patients. We observed more 3R tau inclusions per astrocyte and more astrocytes with 3R tau inclusions in AD patients than in controls. Furthermore, this accumulation was greater in patients presenting hyperphosphorylated tau and was exacerbated when the hilus exhibited amyloid plaques (**Fig. 2a-d**). In contrast, no change in astrocytic accumulation of 4R tau was found with disease state (**Fig. 2e-g**). In the non-astrocytic ($S100\beta^-$) compartment, we found a great variability of 3R and 4R tau accumulation, which was not associated with disease state (**Data Extended Fig.3 a-d**).

The increased accumulation of 3R tau in astrocytes with disease state was not due to modifications of S100β expression, since the density of $S100\beta^+$ cells was similar between patients and control donors (**Data Extended Fig. 3 e-h**). Thus, disease state is associated with 3R tau accumulation in hilar astrocytes.

Synaptic failure is a major hallmark of AD resulting in a decrease[9], or an increase in the density of synaptic proteins[10], depending on disease state and reactive mechanisms. We therefore assessed

96 the expression of the presynaptic protein synaptophysin and the postsynaptic protein PSD95 using
97 immunohistochemistry. The density of PSD95 (**Fig. 2h,i**) but not of the presynaptic protein
98 synaptophysin (**Data Extended Fig. 4**) was significantly increased in the hilus of AD patients
99 presenting hyperphosphorylated tau, an effect that was exacerbated by the presence of amyloid
100 plaques. The density of PSD95 immunostaining greatly correlated with the proportion of astrocytes
101 accumulating 3R but not 4R tau, suggesting a link between 3R tau accumulation in astrocytes and
102 synaptic alterations **(Fig. 2j,k)**. Thus in AD, the hilus of the dentate gyrus is particularly responsive
103 to disease progression and astrocytes accumulate 3R tau, which is associated with synaptic
104 alterations and the severity of the pathology.
105

106 **Viral strategy for expressing tau in hilar astrocytes of adult mice**

107 Our observations from human samples raise the possibility that 3R tau accumulation in hilar
108 astrocytes may participate to hippocampal dysfunction and disease etiology. To test this possibility,
109 we developed a novel lentiviral vector (LV) to specifically target astrocytes. We used a truncated
110 version of the GFAP promoter, named gfaABC1D promoter[11], with a B3 enhancer (gfaABC1D(B3),
111 hereafter called G1) and the previously-described miR124T neuronal detargeting system [12] (LV-
112 G1-GFP, **Fig. 3a**). To assess the astrocytic specificity of this construct in the adult mouse brain, we
113 injected the reporter LV-G1-GFP in the hilus of the dentate gyrus of adult mice. Two weeks after
114 injection, we examined the distribution and identity of the GFP-expressing cells. All GFP^+ cells
115 were found in the dentate gyrus, with a majority (68.4 ± 1.7%), in the hilus (**Fig. 3b-c**). Regardless
116 of their position, virtually all GFP^+ cells expressed GFAP (**Fig. 3d**) and S100β (**Fig. 3e**), which are
117 astrocytic markers. Adult hippocampal stem cells that reside in the subgranular zone of the dentate
118 gyrus also express GFAP and could potentially be targeted by the LV. To assess stem cell
119 targeting, we injected another set of mice. Four days after LV injection, 8.1 ± 2.1% of GFP^+ cells
120 exhibited radial glial-like stem cell morphology, with a soma in the subgranular zone and a radial
121 process extending into the granule cell layer (**Data Extended Fig. 5**), suggesting that few adult
122 neural stem cells may have been targeted by the LV. These cells represented 11 ± 1.2% of all
123 radial-glial like cells and this proportion decreased to 3.0% ± 1.1% at 14 and 120 days after LV
124 injection. Furthermore, only 0.4 ± 0.4% of GFP^+ cells expressed the mature neuronal marker NeuN
125 (**Fig. 3f**), suggesting that the neuronal detargeting system disabled the transgene expression in
126 new neurons as they matured. Together, these results show that this approach enabled the
127 specific targeting of hilar astrocytes in the mouse hippocampus.
128 We next used this strategy to express the human tau isoforms in astrocytes. Since tau 0N is a fetal
129 isoform and tau 2N is weakly expressed in the human brain[13], we used the 1N (1N3R and 1N4R)
130 isoforms linked to a V5 tag (LV-G1-1N3R or LV-G1-1N4R; **Fig. 3g**). We previously reported that
131 the V5 tag does not interfere with tau protein hyperphosphorylation and misfolding[14] and it enables
132 the detection of exogenous tau by western blot (**Fig.3h**) and immunohistochemistry (**Fig.3i**). Four
133 months after the co-injection of LV-G1-GFP and either LV-G1-1N3R or LV-G1-1N4R in the dorsal

134 hippocampus, approximatively 500 hilar cells per hippocampus were infected (**Fig. 3j).** All
135 transduced cells were found in the dentate gyrus, with a majority (65%) in the hilus. Similarly to the
136 LV-G1-GFP reporter construct, virtually all transduced cells were identified as astrocytes (**Fig. 3k**),
137 representing half of the astrocyte population in the dorsal hilus (**Fig. 3l**). Astrocytes that
138 accumulated human 1N3R or 1N4R tau exhibited a pathological conformation of tau, as assessed
139 by immunohistochemistry using the MC-1 antibody[15], (**Data Extended Fig. 6a**).
140 Thus, this LV enables the long-term expression of the human tau isoforms in astrocytes of the
141 dentate gyrus and in particular the hilus, with very high anatomical and cellular specificity.
142

143 Tau isoforms overexpression in astrocytes differentially affects mitochondria 144 distribution and function

145 By enabling their coupling with the cytoskeleton, tau is known to play a role in organelle distribution
146 and in particular, in mitochondria transport[16]. To assess the consequences of tau isoforms
147 accumulation on mitochondria*,* we used MitoTimer[17]. To examine the effect of 1N3R or 1N4R tau
148 isoforms on mitochondria, we co-injected, in the mouse dentate gyrus, the following combinations
149 of LV: LV-G1-MitoTimer + LV-G1-CFP + LV-G1-1N3R-V5 or LV-G1-MitoTimer + LV-G1-CFP + LV-
150 G1-1N4R-V5, or as control, LV-G1-MitoTimer + LV-G1-CFP (or LV-G1-GFP). Four months after
151 injection, most astrocytes infected with the control construct (LV-G1-CFP) exhibited a uniform
152 distribution of mitochondria in the soma, proximal processes (between 1 and 20 µm from the
153 soma) and distal processes (more than 20 µm from the soma), which was defined as a class 1-
154 distribution pattern. A few astrocytes (17.0 ± 9% of all control astrocytes) were devoid of
155 mitochondria in the distal processes (defined as a class 2 distribution pattern) or in distal and
156 proximal processes (defined as a class 3 distribution pattern; 14.5 ± 2% of all control astrocytes,
157 **Fig. 4a,b**). In contrast, 1N3R tau overexpression strongly reduced the number of mitochondria
158 located in the distal processes, as evidenced by a significant increase in the proportion of class 3
159 and decrease in class 1 astrocytes (**Fig. 4b, Data Extended Fig. 6b-d)**. 1N4R also induced a
160 redistribution of mitochondria towards the soma, albeit less drastic than 1N3R (**Fig. 4b**).
161 Mitochondrial relocation towards the soma may be due to a retraction of astrocytic processes. To
162 test this possibility, we analyzed the effect of 1N3R or 1N4R tau on astrocytic morphology. We
163 found that 1N3R and 1N4R tau, were homogeneously distributed throughout the soma and
164 processes of astrocytes (**Fig. 4c**). Furthermore, using GFP to examine astrocyte morphology, we
165 found that the projected area of individual astrocytic territories, the area of the soma, the number of
166 branching points, the number of segments, the number of terminal points, the total length of
167 processes and neuropil infiltration volume (**Fig.4 d,k**) were similar between control and 1N3R or
168 1N4R astrocytes. Together, these results indicate that 1N3R and to a lesser extent 1N4R, induce a
169 redistribution of mitochondria from the processes towards the soma without modifying the
170 morphology of astrocytes.

171 Next, we used the 555nm/488nm fluorescence ratio to examine the turnover and redox state of
172 individual mitochondria. Both 1N3R and 1N4R tau increased the 555nm/488nm fluorescence ratio
173 of mitochondria (**Fig. 4 l,m**), indicating a reduced turnover and increased oxidized state of
174 mitochondria.
175 In order to further investigate the consequences of 1N3R and 1N4R tau isoforms overexpression in
176 astrocytes on mitochondrial dynamics and function, we used rat hippocampal neuron-glial co-
177 cultures infected with the following combination of LV: LV-G1-MitoTimer + LV-G1-CFP as control,
178 or LV-G1-MitoTimer + LV-G1-CFP + LV-G1-1N3R or LV-G1-MitoTimer + LV-G1-CFP + LV-G1-
179 1N4R. Similarly to our *in vivo* observations, the LV targeted almost exclusively astrocytes and most
180 astrocytes were co-infected (**Data Extended Fig. 7a-d**). Likewise, we found that mitochondria in
181 control conditions were uniformly distributed between proximal (between 1 and 20 µm from the
182 soma) and distal processes (more than 20 µm from the soma) of astrocytes (**Fig. 5a-c**). In
183 contrast, 1N3R tau induced a drastic relocation of mitochondria in proximal processes, whereas
184 1N4R did not change the distribution of mitochondria in astrocytes (**Fig. 5c**). Here too, tau isoforms
185 did not induce morphological changes of astrocytes. (**Data Extended Fig. 7e-k**).
186 The effect of 1N3R tau on mitochondria distribution may be due to an effect on motility and
187 dynamics. To assess this possibility, we used confocal live imaging to track mitochondria
188 movement and found that 1N3R but not 1N4R increased the proportion of stationary mitochondria
189 **(Fig. 5d, Supplementary Video 1, 2)**. Furthermore, by observing the movement of mitochondria
190 relative to the soma, we found that 1N3R but not 1N4R reduced the anterograde and increased the
191 retrograde movement of mitochondria (**Fig. 5e**). Thus, 1N3R tau reduced the total motility of
192 mitochondria and induced their transfer to the soma, resulting in a decrease in mitochondria in the
193 distal segments of astrocytic processes.
194 Movement enables the recycling of damaged mitochondria, their fusion and fission as well as
195 biogenesis, all of which sustain mitochondria function[18]. We therefore expected the scarce,
196 stationary, distal mitochondria to exhibit morphological and functional impairment. We first
197 examined the morphology of individual mitochondria. As compared to control conditions, 1N3R but
198 not 1N4R tau overexpression in astrocytes reduced mitochondria projected area, especially in the
199 distal processes (**Fig. 5f**), suggesting that the mitochondria that remained in the distal processes
200 may be impaired. Next, we examined the redox state / turnover of mitochondria using the using the
201 MitoTimer reporter gene. Neither 1N3R nor 1N4R altered the turnover / redox state of mitochondria
202 in the soma. However, both isoforms increased the redox state in the mitochondria that had
203 remained in the proximal and distal processes (**Fig. 5g, h**). Thus, the *in vitro* experiments
204 confirmed and extended the *in vivo* observations showing that 1N3R tau overexpression in
205 astrocytes induced mitochondria relocation in the soma, concomitant with alterations in
206 mitochondria morphology and function in the distal processes, whereas 1N4R had a modest
207 impact, restricted to mitochondria motility and redox state.

208 In astrocytes, mitochondria dynamics and redox state / turnover have an impact on intracellular
209 ATP production and the regulation of intracellular calcium concentration[19]. In order to investigate
210 the consequences of 1N3R and 1N4R tau overexpression in astrocytes on mitochondrial ATP
211 production, we used a FRET-based sensor for ATP production. To this aim, we co-infected
212 astrocytes-neurons co-cultures with an LV encoding either the cyan fluorescent protein (LV-G1-
213 CFP as control) or LV-G1-1N3R or LV-G1-1N4R, together with a LV coding for Forster Resonance
214 Energy Transfer (FRET) - based fluorescent mitochondrial ATP probe[20] (LV-G1-MitoGoAteam2). In
215 astrocytes overexpressing 1N3R tau but not in astrocytes overexpressing 1N4R tau, we found that
216 ATP production by individual mitochondria was significantly reduced in distal processes as
217 compared to control astrocytes (**Fig. 5i,j**). In contrast, we found no difference in ATP production in
218 mitochondria of the soma or proximal processes (**Fig. 5j**). Finally, we investigated the calcium
219 concentration in the soma and proximal and distal processes using the Fluo 4AM calcium sensor.
220 Compared to control, 1N3R tau overexpression had no impact on calcium concentration in the
221 soma and proximal processes but significantly decreased calcium concentrations in distal
222 processes, whereas 1N4R did not influence calcium concentrations (**Fig. 5k,l)**. Overall, these
223 results show that *in vitro*, 1N3R tau overexpression in astrocytes induced the relocation of
224 mitochondria from the distal processes to the soma and proximal processes, which resulted in few
225 and impaired distal mitochondria. In contrast, 1N4R showed mild effects on mitochondria
226 localization and did not impair mitochondrial function. We therefore next focused on the functional
227 implications of 1N3R overexpression.
228
229 **1N3R tau overexpression in hilar astrocytes impairs the hippocampal neuronal network**
230
231 To assess the long-term consequences of 1N3R tau accumulation in hilar astrocytes on neurons,
232 we injected LV-G1-CFP (control) or LV-G1-1N3R + LV-G1-CFP in the hilus of adult mice. Four
233 months later, we evaluated the density of different neuronal populations in the hilus. In both
234 conditions, we observed a similar density of cells ($DAPI^+$, **Fig. 6a**) and of neurons in the hilus
235 ($NeuN^+$, **Fig. 6b**), suggesting that 1N3R tau overexpression in astrocytes did not induce cell death.
236 In contrast, 1N3R tau overexpression in astrocytes significantly decreased the number of neurons
237 expressing the activity-dependent protein parvalbumin (PV, **Fig. 6c**), whereas the density of mossy
238 cells was not changed ($GluR2/3^+$, **Fig. 6d**). This suggests that 1N3R tau overexpression in
239 astrocytes affected PV expression in interneurons and consequently, reduced the inhibitory
240 transmission. The dentate gyrus is one of the two major sites for adult neurogenesis to occur and a
241 dysregulation of astrocytes or neuronal activity may interfere with this process[21] .We quantified cell
242 proliferation by injecting animals with the thymidine analog 5-bromo-2-deoxy-uridine (BrdU) and
243 analyzing animals one day after BrdU injection. We found that the number of cells that
244 incorporated BrdU in the subgranular zone was unchanged in 1N3R tau-overexpressing animals
245 (**Fig. 6e**), suggesting that the few radial glia-like cells that were targeted by the LV (**Data Extended**

246 **Fig. 5**) were not sufficient to influence cell proliferation in the dentate gyrus. To assess the later
247 stages of adult neurogenesis, we used immunostaining against the cytoskeletal marker of
248 immature neurons, doublecortin. The number of doublecortin-expressing cells was significantly
249 reduced in 1N3R tau-expressing animals (**Fig. 6f**), suggesting an impaired maturation of newborn
250 neurons.
251 Next, we examined inhibitory synapses in the hilus. Inhibitory synapses are composed of
252 nanoscale subsynaptic domains where the scaffolding protein gephyrin and the GABA vesicle
253 transporter VGAT are closely associated (within 300 nm of each other[22]). Using three-dimensional
254 confocal reconstructions, we evaluated the density of VGAT and gephyrin clusters in the territories
255 of 1N3R-overexpressing astrocytes (**Fig. 6g-h**). As compared to control mice, we observed a
256 decrease in gephyrin dots, resulting in a reduction of paired VGAT-gephyrin punctae, which
257 indicates a reduction of inhibitory synapses (**Fig. 6i-l**). Thus, the overexpression of 1N3R tau in
258 astrocytes impaired inhibitory neurons and adult neurogenesis.
259 Together, these results suggest that 1N3R tau overexpression in astrocytes may impair the
260 function of the neuronal network in the hilus of the dentate gyrus. To assess the basal activity of
261 the hilus, we examined the expression of the immediate-early gene c-fos. LV-G1-1N3R-injected
262 animals showed fewer c-fos^{+} cells in the hilus than control mice, suggesting reduced neuronal
263 activity in the hilus of these mice **(Fig. 6m)**. Parvalbumin-expressing interneurons are crucial for
264 the generation of gamma oscillations, which enable coincidence detection and regulate circuit
265 performance[23]. We therefore examined evoked gamma oscillations in the dentate gyrus of acute
266 hippocampal slices using extracellular electrophysiological recordings. Transient high frequency
267 oscillatory activity was induced by a brief focal application of glutamate in the hilus (**Fig 6n-t**)[24]. We
268 observed two distinct types of oscillatory activity: A gamma oscillatory activity (mean peak
269 frequency ~75 Hz) which relies on functional GABAA receptor transmission (**Fig. 6o-q**)[24,25] and a
270 faster oscillatory activity (mean peak frequency ~100 Hz), similar to the non-synaptic network
271 synchrony described by Towers et al.[25] **(Fig 6r-t)**. In slices obtained from mice injected with the LV-
272 G1-1N3R vector, we found that the power of gamma oscillations (within the range of 50 to 90 Hz)
273 was significantly reduced as compared to slices from control mice **(Fig.6q).** Likewise, the peak
274 frequency of these gamma oscillations was significantly lower in 1N3R tau mice (68.6 ± 1.6 Hz,
275 mean ± sem) than in control mice (75.1 ± 1.3, $p<0.01$, **Fig.6p**). In contrast, we observed no
276 significant difference in the power and the peak frequency of the faster oscillatory activity **(Fig.6s)**.
277 Thus, the accumulation of human 1N3R tau in hilar astrocytes impaired synchronous activity.

278

279 **Hilar astrocytic 1N3R tau accumulation affects spatial memory of adult mice**

280 Gamma oscillations in the dentate gyrus play a role in spatial memory[26] and are impaired in mouse
281 models of Alzheimer's disease[27]. We therefore compared the hippocampal-dependent spatial
282 memory performances of mice 4 months after the bilateral injection of LV-G1-CFP as control, or

LV-G1-1N3R LV (**Fig. 7a**). We first used the novel object location task and found that the preference index for the displaced object was significantly higher than chance level for the control but not for the LV-G1-1N3R group, indicating a reduction of spatial memory (**Fig. 7b-d)**. On another set of mice, we performed the Morris water maze test. LV-G1-1N3R-injected mice showed similar performances to control mice in the learning phase and the probe test (**Fig. 7e-g**). However, they showed a deficit in reversal memory (**Fig. 7h-i**), indicating a difficulty to suppress old spatial memory. To assess whether the decreased performances were specific to spatial memory, four independent behavioral tests, non related to spatial memory, were performed on the same sets of mice: dark/light box test, which assesses anxiety, Y-maze (YM) for spatial working memory, object recognition task (OR) for non-spatial long-term memory, and contextual fear conditioning, which assesses fear memory. For all these tests, LV-G1-1N3R-injected mice performed similarly to control mice (**Data Extended Fig. 8**). Thus, the long-term overexpression of 1N3R tau in hilar astrocyte is sufficient to specifically alter spatial memory.

PV interneurons play an important role in hippocampal function and spatial memory[28]. However, it is unclear whether the reduction of PV interneurons observed after 1N3R tau overexpression in astrocytes participates to the behavioral impairment observed in these mice. To test this possibility, we used the neuregulin 1 peptide (NRG1p*)* to increase PV interneuron excitability[29]. Another set of animals was injected with LV-G1-1N3R or LV-G1-GFP. Four months later, mice were injected with NRG1p or vehicle and, 1 hour later, tested on the novel object location test. Similarly to the cohort of mice shown in Fig. 7d, 1N3R tau-vehicle injected mice showed a lack of preference for the displaced object, as compared to control groups. The recognition of the displaced object was however restored in LV-G1-1N3R animals injected with NRG1p (**Fig. 7j**), suggesting that increasing PV interneurons activity restored the effect of 1N3R tau expression in astrocytes. To assess the involvement of PV interneurons in this effect, we examined PV immunoreactivity immediately after the behavioral test. LV-G1-1N3R-injected mice showed a reduced number of PV^+ cells and a reduced density of PV immunoreactivity in the hilus as compared to controls groups and the density of PV immunoreactivity was restored to control values upon NRG1p injection (**Fig. 7k-n**).

Thus, 1N3R tau expression in hilar astrocytes reduced long-term, spatial memory performances, which were restored upon stimulation of PV interneurons by NRG1p injection.

Discussion

We found that in AD patients, astrocytes of the hilus of the dentate gyrus accumulate 3R but not 4R tau, and this accumulation is correlated with synaptic alterations, suggesting an important role for astrocytes in disease progression. Using a novel LV to specifically target astrocytes of the hilus, we found that overexpression of the human 1N3R isoform of tau in these cells strongly impaired mitochondrial motility, distribution and function, resulting in impaired neurogenesis, reduced number of neurons expressing parvalbumin, decreased density of inhibitory synapses, and

321 reduced gamma oscillatory activity. Together, these modifications led to impaired spatial memory,
322 which was restored by stimulating PV interneuron activity.
323 Although tau has been found in glial cells[30], astrocytes do not express this protein in physiological
324 conditions[31], and the origin of tau in astrocytes in AD is unclear. One unsubstantiated possibility is
325 that AD progression induces tau translation from the mRNA present in astrocytes[32]. Alternatively,
326 astrocytes may capture extracellular tau. Indeed, tau is released in the interstitial fluid by
327 neurons[33], spreads between cells[34] and astrocytes can uptake tau when exposed to this protein[35].
328 Furthermore, tau was found in extracellular vesicles from the cerebrospinal fluid of AD patients[36]
329 which may also contribute to the intercellular propagation of this protein[37,38]. These possibilities are
330 currently under intense scrutiny.
331 In tauopathies, much attention has been given to the role of tau in neurons[39]. However, in many
332 tauopathies, tau is found in glial cells[40], with poorly-known consequences for disease symptoms
333 and progression. Disentangling the contribution of different cell types to a given phenotype is
334 crucial for our understanding of disease aetiology. However, access to this information is often
335 hampered by the lack of specific tools that selectively target subpopulations of cells. Similarly, the
336 contribution of small brain regions to specific functions is difficult to assess without tools that
337 selectively target them. In this study, we achieved the first goal by using a novel LV strategy which
338 enabled the expression of the genes of interest in astrocytes, with negligible expression in non-
339 astrocytic cell types, both *in vitro* and *in vivo*. Upon injection into the hilus, the limited diffusion of
340 the LV further enabled the exclusive targeting of the dentate gyrus, since all transduced cells were
341 found in the dentate gyrus and about 70% in the hilus. This targeting, both at the anatomical and at
342 the cellular levels, enabled us to reproduce in mice, the observations we obtained from human
343 patients.
344 Using this approach, we found that 1N3R and 1N4R tau overexpression in astrocytes differentially
345 altered their mitochondrial localization, trafficking and function, as well as calcium buffering. These
346 effects may be mediated by several mechanisms: First, tau competes with kinesin/dynein cargoes
347 for microtubules, which are involved in mitochondria transport in astrocytes[41]. Interestingly, tau
348 affinity for microtubules differs between the 3R and 4R isoforms[42], a difference that may underlie
349 their differential effect on astrocytic mitochondria. Furthermore, according to models of multiple-
350 motor driven cargo transport[43], the higher solubility and kinesin inhibitory activity[44] of 3R tau
351 compared to 4R tau may induce a strong steric inhibition of the binding strength of mitochondria to
352 microtubules, leading to their immobilization. Alternatively, the effect of tau on mitochondrial
353 transport may be due to post-translational modifications, such as phosphorylation or truncation,
354 which modulate tau functions. Indeed, tau truncation produces N-terminal fragments, which
355 modulate kinesin velocity[45] and overexpression of N-terminal tau fragments alters the
356 mitochondrial system[46]. Furthermore, tau overexpression in astrocytes disrupts the intermediate
357 filament network[47], which may impair the transport of other cargo, including peroxysomes and
358 endosomes[48], disrupts the blood-brain barrier[49], reduces the expression of glutamate transporters[50]

359 and reduces gliotransmitter release[51]. Alone or in combination, these effects are consistent with
360 our observations of impaired mitochondrial transport and function. In turn, since astrocytes are
361 involved in diverse brain functions[52], the impairment of astrocytic function is expected to impact on
362 the neuronal network and on behavior.
363 It is noteworthy that the impairment of a few hundreds of astrocytes in the hilus of the dentate
364 gyrus altered hippocampal function and spatial memory. Although our results do not rule out that
365 other brain areas may display astrocytic tau accumulation in the course of AD, the dentate gyrus is
366 crucial for hippocampal function and memory performances[53]. In particular, our results point to two
367 major effects of disrupted astrocytes on the function of the dentate gyrus: Adult neurogenesis and
368 PV interneuron function. Adult neurogenesis occurs in several steps, from stem/progenitor cell
369 proliferation to the differentiation and maturation of new neurons, several of which are regulated by
370 astrocytes[54]. Here, we found that 1N3R tau expression in astrocytes did not affect proliferation, but
371 strongly reduced the number of immature neurons, similarly to recent observations in the human
372 AD brain[55]. These results are consistent with the role of gliotransmitters in the maturation of adult-
373 born hippocampal neurons[21]. Since immature granule neurons play a role in hippocampal-
374 dependent memory[56], their reduction may participate to the memory impairment in LV-G1-1N3R-
375 injected mice. PV interneurons also play a great role in hippocampal function. By exerting an
376 important control over granule neurons, they fine-tune their activity and enable pattern
377 separation[57]. Furthermore, PV interneurons enable the generation of gamma oscillations, which
378 support coincidence detection and regulate circuit performance[59]. The strong reduction of PV
379 immunostaining in LV-G1-1N3R-injected mice suggests that PV interneurons likely underlie their
380 memory impairments, a possibility that is further supported by the NRG1p-mediated behavioral
381 rescue.
382 Astrocytes are key actors in brain physiology and play a fundamental role in the regulation of
383 neural functioning[60] and adult neurogenesis[21]. Our observations suggest that these cells may play
384 a greater role than expected in AD. Although the extent to which astrocytes are involved in the
385 etiology of AD remains unclear, our results show that their impairment can contribute to memory
386 disturbances and may dramatically worsen disease symptoms.

387

388 Acknowledgements

389 This study was supported by a Synapsis Foundation fellowship awarded to K. R. and the Lausanne
390 University Hospital (CHUV) and by the Swiss National Science Foundation (31003A_173128 to
391 N.T and K.R.). L.B., M.C, S.H, R.C and S.E were supported by the Programme Investissement
392 d'avenir LabEx (laboratory excellence) DISTALZ (Development of Innovative Strategies for a
393 Transdisciplinary approach to ALZheimer's disease), France Association PSP, the LiCEND (Lille
394 Centre of Excellence in Neurodegenerative Disorders), CNRS, Inserm, Métropole Européenne de

Lille, Univ. Lille, FEDER and DN2M. The authors would like to thank the Cellular Imaging Facility of the University of Lausanne for their technical support, Dr. Fulvio Magara at the Center for Behavioral Studies of the Lausanne University Hospital, for assistance with the behavioral testing, Dr. Hiromi Imamura of Kyoto University - Japan for the MitoGoAteam2 plasmid. We warmly thank Pr. Claire Rampon and Pr. Marie Christine Miquel at the University of Toulouse and Gabriel Vachey, Dr. Marie Humbert-Claude, Dr. Liliane Tenenbaum and Dr. Raoul Jenni at the Lausanne University Hospital for their precious help. We also thank Dr. Sebastien Sultan, Dr. Frederic Cassé and Dr. Thomas Larrieu for their critical reading of the manuscript and helpful comments.

Contributions

K.R conceived the project and co-supervised the study, acquired and analyzed the data, and wrote the manuscript. G.L. collected human samples and performed immunostainings. M.P and R.P. acquired and analyzed some microscopy data. M.M acquired the data for LV tropism. P.B. designed the calcium imaging experiments. P.S. and K.D. designed and performed the electrophysiology experiments. M.R cloned the plasmids and produced the LV. C.P., E.P. and R.C. produced the *in vitro* cultures and immunohistochemistry. S.H, S.B. and MC acquired and analyzed data. M.C, L.B, helped with the research design and critically revised the manuscript. N.T designed and supervised the study and wrote the manuscript. N.D. designed the lentiviral vectors and supervised the study.

Competing interests

The authors declare no competing interests.

417 ## References

418 1. Buee, L. *et al.* Tau protein isoforms, phosphorylation and role in neurodegenerative
419 disorders. *Brain Res. Rev.* **33**, 95–130 (2000).

420 2. Adams, S. J., de Ture, M. A., McBride, M., Dickson, D. W. & Petrucelli, L. Three repeat
421 isoforms of tau inhibit assembly of four repeat tau filaments. *PLoS One* **5**, (2010).

422 3. Panda, D., Samuel, J. C., Massie, M., Feinstein, S. C. & Wilson, L. Differential regulation of
423 microtubule dynamics by three- and four-repeat tau: Implications for the onset of
424 neurodegenerative disease. *Proc. Natl. Acad. Sci.* **100**, 9548–9553 (2003).

425 4. Conrad, C. C. *et al.* Single molecule profiling of tau gene expression in Alzheimer's disease.
426 *J. Neurochem.* **103**, 1228–1236 (2007).

427 5. Hamilton, L. K. *et al.* Aberrant Lipid Metabolism in the Forebrain Niche Suppresses Adult
428 Neural Stem Cell Proliferation in an Animal Model of Alzheimer's Disease. *Cell Stem Cell*
429 **17**, 397–411 (2015).

430 6. Santello, M., Toni, N. & Volterra, A. Astrocyte function from information processing to
431 cognition and cognitive impairment. *Nature Neuroscience* **22**, 154–166 (2019).

432 7. Buée-Scherrer, V. *et al.* AD2, a phosphorylation-dependent monoclonal antibody directed
433 against tau proteins found in Alzheimer's disease. *Mol. Brain Res.* **39**, 79–88 (1996).

434 8. Gabor G. Kovacs, Isidro Ferrer, Lea T. Grinberg, Irina Alafuzof Johannes Attems, Herbert
435 Budka, Nigel J. Cairns, John F. Crary, Charles Duyckaerts, Bernardino Ghetti, Glenda M.
436 Halliday, James W. Ironside, Seth Love, Ian R. Mack, J. C. Aging-related tau astrogliopathy
437 (ARTAG): harmonized evaluation strategy. **2**, 87–102 (2015).

438 9. Bereczki, E. *et al.* Synaptic proteins predict cognitive decline in Alzheimer's disease
439 and Lewy body dementia. *Alzheimers. Dement.* **12**, 1149–1158 (2016).

440 10. Savioz, A., Leuba, G. & Vallet, P. G. A framework to understand the variations of PSD-95
441 expression in brain aging and in Alzheimer's disease. *Ageing Res. Rev.* **18**, 86–94 (2015).

442 11. Lee, Y., Messing, A., Su, M. & Brenner, M. GFAP promoter elements required for region-
443 specific and astrocyte-specific expression. *Glia* **56**, 481–493 (2008).

444 12. Colin, A. *et al.* Engineered lentiviral vector targeting astrocytes in vivo. *Glia* **57**, 667–679
445 (2009).

446 13. Boutajangout, A., Boom, A., Leroy, K. & Brion, J. P. Expression of tau mRNA and soluble

447 tau isoforms in affected and non-affected brain areas in Alzheimer's disease. *FEBS Lett.*
448 **576**, 183–9 (2004).

449 14. Dujardin, S. *et al.* Neuron-to-neuron wild-type Tau protein transfer through a trans-synaptic
450 mechanism: relevance to sporadic tauopathies. *Acta Neuropathol Commun* **2**, 14 (2014).

451 15. Jicha, G. A., Bowser, R., Kazam, I. G. & Davies, P. Alz-50 and MC-1, a new monoclonal
452 antibody raised to paired helical filaments, recognize conformational epitopes on
453 recombinant tau. *J. Neurosci. Res.* **48**, 128–132 (1997).

454 16. Cheng, Y. & Bai, F. The association of tau with mitochondrial dysfunction in Alzheimer's
455 disease. *Front. Neurosci.* **12**, 2014–2019 (2018).

456 17. Gottlieb, R. a. & Stotland, A. MitoTimer: a novel protein for monitoring mitochondrial
457 turnover in the heart. *J. Mol. Med.* **93**, 271–278 (2015).

458 18. Eisner, V., Picard, M. & Hajnóczky, G. Mitochondrial dynamics in adaptive and maladaptive
459 cellular stress responses. *Nature Cell Biology* **20**, 755–765 (2018).

460 19. Agarwal, A. *et al.* Transient Opening of the Mitochondrial Permeability Transition Pore
461 Induces Microdomain Calcium Transients in Astrocyte Processes. *Neuron* **93**, 587-605.e7
462 (2017).

463 20. Nakano, M., Imamura, H., Nagai, T. & Noji, H. Ca(2+) regulation of mitochondrial ATP
464 synthesis visualized at the single cell level. *ACS Chem. Biol.* **6**, 709–15 (2011).

465 21. Sultan, S. *et al.* Synaptic Integration of Adult-Born Hippocampal Neurons Is Locally
466 Controlled by Astrocytes. *Neuron* **88**, 957–972 (2015).

467 22. Crosby, K. C. *et al.* Nanoscale Subsynaptic Domains Underlie the Organization of the
468 Inhibitory Synapse. *Cell Rep.* **26**, 3284-3297.e3 (2019).

469 23. Cardin, J. A. *et al.* Driving fast-spiking cells induces gamma rhythm and controls sensory
470 responses. *Nature* **459**, 663–667 (2009).

471 24. Pöschel, B., Heinemann, U. & Draguhn, A. High frequency oscillations in the dentate gyrus
472 of rat hippocampal slices induced by tetanic stimulation. *Brain Res.* **959**, 320–327 (2003).

473 25. Towers, S. K. *et al.* Fast network oscillations in the rat dentate gyrus in vitro. *J.*
474 *Neurophysiol.* **87**, 1165–1168 (2002).

475 26. Espinoza, C., Guzman, S. J., Zhang, X. & Jonas, P. Parvalbumin+ interneurons obey unique
476 connectivity rules and establish a powerful lateral-inhibition microcircuit in dentate gyrus.

477 *Nat. Commun.* **9**, 4605 (2018).

478 27. Gillespie, A. K. *et al.* Apolipoprotein E4 Causes Age-Dependent Disruption of Slow Gamma
479 Oscillations during Hippocampal Sharp-Wave Ripples. *Neuron* **90**, 740–751 (2016).

480 28. Hu, H., Gan, J. & Jonas, P. Fast-spiking, parvalbumin+ GABAergic interneurons: From
481 cellular design to microcircuit function. *Science (80-.).* **345**, (2014).

482 29. Marissal, T. *et al.* Restoring wild-type-like CA1 network dynamics and behavior during
483 adulthood in a mouse model of schizophrenia. *Nat. Neurosci.* **21**, 1412–1420 (2018).

484 30. LoPresti, P., Szuchet, S., Papasozomenos, S. C., Zinkowski, R. P. & Binder, L. I. Functional
485 implications for the microtubule associated protein tau: localization in oligodendrocytes.
486 *Proc. Natl. Acad. Sci. U. S. A.* **92**, 10369–73 (1995).

487 31. Müller, R., Heinrich, M., Heck, S., Blohm, D. & Richter-Landsberg, C. Expression of
488 microtubule-asssciated proteins MAP2 and tau in cultured rat brain oligodendrocytes. *Cell*
489 *Tissue Res.* **288**, 239–249 (1997).

490 32. Boisvert, M. M., Erikson, G. A., Shokhirev, M. N. & Allen, N. J. The Aging Astrocyte
491 Transcriptome from Multiple Regions of the Mouse Brain. *Cell Rep.* **22**, 269–285 (2018).

492 33. Yamada, K. *et al.* In vivo microdialysis reveals age-dependent decrease of brain interstitial
493 fluid tau levels in P301S human tau transgenic mice. *J. Neurosci.* **31**, 13110–13117 (2011).

494 34. Sanders, D. W. *et al.* Distinct tau prion strains propagate in cells and mice and define
495 different tauopathies. *Neuron* (2014). doi:10.1016/j.neuron.2014.04.047

496 35. Perea, J. R. *et al.* Extracellular monomeric tau is internalized by astrocytes. *Front. Neurosci.*
497 **13**, 442 (2019).

498 36. Dujardin, S. *et al.* Ectosomes: A new mechanism for non-exosomal secretion of Tau protein.
499 *PLoS One* **9**, 28–31 (2014).

500 37. Asai, H. *et al.* Depletion of microglia and inhibition of exosome synthesis halt tau
501 propagation. *Nat. Neurosci.* **18**, 1584–1593 (2015).

502 38. Goetzl, E. J. *et al.* Cargo proteins of plasma astrocyte-derived exosomes in Alzheimer's
503 disease. *FASEB J.* **30**, 3853–3859 (2016).

504 39. Wang, Y. & Mandelkow, E. *No Title*. **17**, 5–21 (Nature Publishing Group, 2016).

505 40. Ferrer, I. *et al.* Aging-related tau astrogliopathy (ARTAG): not only tau phosphorylation in

506 astrocytes. *Brain Pathol.* **28**, 965–985 (2018).

507 41. Stephen, T. L. *et al.* Mitochondrial dynamics in astrocytes. *Biochem Soc Trans* **42**, 1302–
508 1310 (2014).

509 42. Goode, B. L., Chau, M., Denis, P. E. & Feinstein, S. C. Structural and functional differences
510 between 3-repeat and 4-repeat tau isoforms: Implications for normal tau function and the
511 onset of neurodegenerative disease. *J. Biol. Chem.* **275**, 38182–38189 (2000).

512 43. Vershinin, M., Carter, B. C., Razafsky, D. S., King, S. J. & Gross, S. P. Multiple-motor based
513 transport and its regulation by Tau. *Proc. Natl. Acad. Sci. U. S. A.* **104**, 87–92 (2007).

514 44. Dixit, R., Ross, J. L., Goldman, Y. E. & Holzbaur, E. L. F. Differential Regulation of Dynein
515 and Kinesin Motor Proteins by Tau. *Science (80-.).* **319**, 1086–1089 (2010).

516 45. Tarhan, M. C., Orazov, Y., Yokokawa, R., Karsten, S. L. & Fujita, H. Biosensing MAPs as
517 'roadblocks': kinesin-based functional analysis of tau protein isoforms and mutants using
518 suspended microtubules (sMTs). *Lab Chip* **13**, 3217–3224 (2013).

519 46. Amadoro, G. *et al.* AD-linked, toxic NH2 human tau affects the quality control of
520 mitochondria in neurons. *Neurobiol. Dis.* **62**, 489–507 (2014).

521 47. Yoshiyama, Y., Zhang, B., Bruce, J., Trojanowski, J. Q. & Lee, V. M.-Y. Reduction of
522 detyrosinated microtubules and Golgi fragmentation are linked to tau-induced degeneration
523 in astrocytes. *J. Neurosci.* **23**, 10662–10671 (2003).

524 48. van Bergeijk, P., Adrian, M., Hoogenraad, C. C. & Kapitein, L. C. Optogenetic control of
525 organelle transport and positioning. *Nature* **518**, 111–4 (2015).

526 49. Forman, M. S. Transgenic Mouse Model of Tau Pathology in Astrocytes Leading to Nervous
527 System Degeneration. *J. Neurosci.* **25**, 3539–3550 (2005).

528 50. Dabir, D. V. Impaired Glutamate Transport in a Mouse Model of Tau Pathology in
529 Astrocytes. *J. Neurosci.* **26**, 644–654 (2006).

530 51. Piacentini, R. *et al.* Reduced gliotransmitter release from astrocytes mediates tau-induced
531 synaptic dysfunction in cultured hippocampal neurons. *Glia* **65**, 1302–1316 (2017).

532 52. Whalley, K. Neurodegenerative disease: Spreading the tau. *Nat. Rev. Neurosci.* **10**, 548–
533 548 (2009).

534 53. Hainmueller, T. & Bartos, M. Dentate gyrus circuits for encoding, retrieval and discrimination
535 of episodic memories. *Nat. Rev. Neurosci.* **21**, 1–16 (2020).

536 54. Cope, E. C. & Gould, E. Adult Neurogenesis, Glia, and the Extracellular Matrix. *Cell Stem*
537 *Cell* **24**, 690–705 (2019).

538 55. Moreno-Jiménez, E. P. *et al.* Adult hippocampal neurogenesis is abundant in neurologically
539 healthy subjects and drops sharply in patients with Alzheimer's disease. *Nat. Med.* **25**, 554–
540 560 (2019).

541 56. Toda, T., Parylak, S. L., Linker, S. B. & Gage, F. H. The role of adult hippocampal
542 neurogenesis in brain health and disease. 1 (2018). doi:10.1038/s41380-018-0036-2

543 57. Trimper, J. B., Galloway, C. R., Jones, A. C., Mandi, K. & Manns, J. R. Gamma Oscillations
544 in Rat Hippocampal Subregions Dentate Gyrus, CA3, CA1, and Subiculum Underlie
545 Associative Memory Encoding. *Cell Rep.* **21**, 2419–2432 (2017).

546 58. Bragin, A. *et al.* Gamma (40-100 Hz) oscillation in the hippocampus of the behaving rat. *J.*
547 *Neurosci.* **15**, 47–60 (1995).

548 59. Sohal, V. S., Zhang, F., Yizhar, O. & Deisseroth, K. Parvalbumin neurons and gamma
549 rhythms enhance cortical circuit performance. *Nature* **459**, 698–702 (2009).

550 60. Bazargani, N. & Attwell, D. Astrocyte calcium signaling: the third wave. *Nat. Neurosci.* **19**,
551 182–189 (2016).

552 ## Figure legends

553 **Figure 1. Tau isoforms accumulation in the hilus of AD patients. (a)** Photomicrographs of the
554 human hippocampus showing the density of hyperphosphorylated tau ($AD2^+$) cells in healthy
555 controls (CTRL) and AD donors. The different areas are indicated as black overlay (ML: Molecular
556 layer, GCL: Granule cell layer of the dentate gyrus). **(b)** Histogram showing the density of $AD2^+$
557 cells in the different hippocampal regions of CTRL and AD donors. **(c)** Correlations between the
558 density of $AD2^+$ cells and Braak stage for each hippocampal area. **(d)** Table showing the
559 correlation and P value between the density of $AD2^+$ cells and Braak stage for each hippocampal
560 area. **(e)** Confocal micrographs showing the inclusions of 3R tau in the hilus of CTRL and AD
561 donors. **(f)** Histogram showing the density of 3R tau inclusions in the hilus of CTRL and AD donors
562 who were categorized according to the presence (+) or absence (-) of hyperphosphorylated tau (P-
563 tau) and Amyloidβ (Aβ). **(g)** Confocal micrographs showing the inclusions of 4R tau in the hilus of
564 CTRL and AD donors. **(h)** Histogram showing the density of 4R tau inclusions in the hilus of CTRL
565 and AD donors who were categorized according to the presence (+) or absence (-) P-tau and Aβ.
566 N=patients/sections per patient; (**b-d**): N=9/4 for Control, N=21/4 for AD), (**f,h**) N=9/4 for Control,
567 N=6/4 for AD ($P\text{-}Tau^-/A\beta^-$), N=6/4 for AD (P-Tau+/Ab-), N=8/4 for AD (P-Tau+/Ab+). Data are
568 presented as the mean ± SEM. Mann-Whitney two-tailed t-test (**b**), one-sided ANOVA with two-

569 tailed Tukey's post-hoc test (**f,h**) and two-tailed Spearman's rank non-parametric correlation test
570 (**d**). Scale bars: 200 µm (**a)** 50 µm (**e,g**).

571 **Figure 2. 3R tau inclusion increase in the hilar astrocytes of AD patients. (a)** Low
572 magnification confocal micrographs of 3R tau (upper panels) or 4R tau inclusions (lower panels) in
573 hilar astrocytes (S100β: green and tau 3R and 4R: red) in CTRL and AD donors. **(b)** Confocal
574 micrographs and orthogonal projections showing the presence of 3R tau inclusions in hilar
575 astrocytes. **(c)** Histogram of the density of 3R tau inclusions in hilar astrocytes of CTRL or AD
576 patients, who were distributed between 3 categories, depending on the presence of
577 phosphorylated tau, amyloid β plaques, or both. **(d)** Histogram of the percentage of astrocytes that
578 contained 3R tau inclusions in CTRL or AD patients. **(e)** Confocal micrographs and orthogonal
579 projections showing the presence of 4R tau inclusions in hilar astrocytes. **(f)** Histogram of the
580 density of 4R tau inclusions in hilar astrocytes of CTRL or AD patients. **(g)** Histogram of the
581 percentage of hilar astrocytes that contained 4R tau inclusions in CTRL or AD patients. **(h)**
582 Photomicrographs showing PSD95 immunostaining in the hilus of CTRL and the 3 categories of
583 AD patients. **(i)** Histogram of the intensity of PSD95 staining in the hilus of CTRL or AD patients. **(j)**
584 Correlation between the intensity of PSD95 staining and the number of hilar astrocytes expressing
585 3R tau. **(k)** Correlation between the intensity of PSD95 staining and the number of hilar astrocytes
586 expressing 4R tau. N=patients/sections per patient/cells per section; (**d,g**): N=8/4/321 for Control,
587 N=6/4/261 for AD (P-Tau$^-$/Aβ$^-$), N=6/4/258 for AD (P-Tau$^+$/Ab$^-$), N=7/4/287 for AD (P-Tau$^+$/Ab$^+$).
588 N=patients/sections per patient; (**i-k**): N=7/4 for Control, N=6/4 for AD (P-Tau$^-$/Aβ$^-$), N=7/4 for AD
589 (P-Tau$^+$/Ab$^-$), N=8/4 for AD (P-Tau$^+$/Ab$^+$). Data are presented as the mean ± SEM. One-sided
590 ANOVA with Tukey's post-hoc test (**c-f,i**) and two-tailed Spearman's rank non-parametric
591 correlation test (**j-k**). Scale bars: 250 µm (**a,h**), 5 µm (**b,e**).

592 **Figure 3. Viral strategy to specifically target hilar astrocytes. (a)** Schematic representation of
593 the VSV-G pseudotyped LV expressing GFP and experimental timeline. Dpi: days post-injection.
594 (**b**) Confocal micrograph of a mouse hippocampus injected with LV-G1-GFP (GFP: green, DAPI:
595 blue), 14 days after LV injection. Inset: a GFP$^+$ astrocyte. **(c)** Histogram showing the distribution of
596 infected (GFP$^+$) cells. (**d-f**) Confocal micrographs and histograms of the distribution of cells that co-
597 expressed GFP with GFAP (**d**), S100β (**e**), or NeuN (**f**). (**g**) Schematic representation of the VSV-G
598 pseudotyped LV and experimental timeline**. (h)** Western blots of hippocampal or cortical punches
599 of animals injected with LV-G1-GFP, LV-G1-1N3R-V5 or LV-G1-1N4R-V5, probed with anti-V5
600 antibody. **(i)** Confocal micrographs of hippocampus of mice injected with LV-G1-GFP, LV-G1-1N3R
601 or LV-G1-1N4 (DAPI: blue, GFP: green, V5: red). **(j)** Histogram of the density of infected cells in
602 the hilus of injected mice for the GFP (white) 1N3R (yellow) or 1N4R (blue) constructs. (**k**)
603 Histogram of the percentage of infected cells with an astrocyte (orange), RGL cell (magenta) or
604 neuron (green) phenotype. **(l)** Histogram of percentage of all S100β$^+$ astrocytes in the hilus of mice
605 that were targeted by each viral construct. Hil: Hilus, GCL: granular cell layer, ML: molecular layer.

606 N=animals/cells per animal. LV-G1-CFP: 4/100-350 (c), LV-G1-1N3R:4/100-350 (c,j), LV-G1-CFP:
607 4/50 (**d-f,k-l**), LV-G1-1N3R:4/50 (**d-f,k-l**), LV-G1-1N4R:4/50 (**d-f,k-l**). Data are presented as the
608 mean ± SEM. Scale bars: 200 µm (**b,i**), 20 µm (**b** inset**, d-f**).

609 **Figure 4. Tau isoforms differentially affect mitochondria in hilar astrocytes *in vivo*. (a)**
610 Representative confocal images of astrocytes displaying the three classes of mitochondria
611 distribution. **(b)** Histogram of the distribution of hilar astrocytes in each class after infection with LV-
612 G1-1N3R, LV-G1-1N4R or control LV. **(c)** Confocal micrographs of hilar astrocytes expressing
613 GFP (left panels) and tau isoforms (red, middle panels) and 3D reconstructions of their soma and
614 processes (right panels). **(d-i)** Morphological quantification of hilar astrocytes transduced with
615 either LV-G1-GFP (white bars), LV-G1-1N3R (yellow) or LV-G1-1N4R (blue) constructs, showing
616 the projected territory are (**d**), surface of the soma (**e**), number of nodes (**f**), number of segments
617 (**g**), number of terminal points (**h**) and total number of processes (**i**). **(j)** Confocal micrographs of
618 hilar astrocytes expressing GFP (green) and tau isoforms (insets, red,) and representative NIVs
619 after 3D reconstructions (magenta). **(k)** Histogram showing the volume occupied by NIVs of
620 astrocytes. **(l)** Confocal micrographs of astrocytes expressing MitoTimer (green and red), after
621 infection with LV-G1-CFP + LV-G1-MitoTimer or LV-G1-1N3R (or LV-G1-1N4R) + LV-G1-CFP +
622 LV-G1-MitoTimer. **(m)** Histogram of the mitochondrial redox state of hilar astrocytes after
623 transduction**.** N=cultures/cells per culture. (**b**): LV-G1-CFP: 5/101, LV-G1-1N3R: 5/106, LV-G1-
624 1N4R: 5/98. (**d-i, k**): LV-G1-CFP: 4/44, LV-G1-1N3R: 4/44, LV-G1-1N4R:4/43. (**m**): LV-G1-CFP:
625 4/205, LV-G1-1N3R: 4/196, LV-G1-1N4R: 5/249. Data are presented as the mean ± SEM. One-
626 sided ANOVA with Tukey's post-hoc test. Scale bars: 20 µm **(a,l)** and 15 µm **(c)**, 10 µm (**j**), 3 µm (**j**,
627 inset).

628 **Figure 5. Tau isoforms differentially alter mitochondrial function in astrocytes *in vitro*. (a)**
629 Schematic representation of hippocampal neuron-glial cultures showing the proximal (<20 µm from
630 the soma) and distal (>20 µm) portions of astrocytic processes. **(b)** Confocal micrographs of
631 mitochondria (white) in astrocytes (blue) 14 days after infection with LV-G1-CFP + LV-G1-
632 MitoTimer (control) or LV-G1-1N3R + LV-G1-CFP + LV-G1-MitoTimer, or LV-G1-1N4R + LV-G1-
633 CFP + LV-G1-MitoTimer. Lower panels: higher magnification views **(c)** Histogram of mitochondria
634 distribution in proximal and distal processes after LV transduction. **(d)** Histogram of the percentage
635 of stationary, mobile, and highly mobile mitochondria after LV transduction, in the proximal (left)
636 and distal (right) processes. **(e)** Histogram of the percentage of anterograde or retrograde
637 mitochondrial motility. **(f)** Histogram of the surface of mitochondria in proximal and distal
638 processes. **(g)** Confocal micrographs of Mito-Timer (green and red) in CFP^+ (blue) astrocytes after
639 expression of CFP alone or CFP and 1N3R or 1N4R tau. (**h**) Histogram of the redox state ratio in
640 the soma, proximal and distal processes after LV transduction. **(i)** Confocal micrographs of Mito-
641 GoAteam2 (green and red) in CFP^+ (blue) astrocytes after expression of CFP alone or CFP and
642 1N3R or 1N4R tau. (**j**) Histogram of the ATP level in the soma, proximal and distal processes of

astrocytes. **(k)** Confocal micrographs of FLUO-4 AM (red) in control CFP^+ (blue) astrocytes and astrocytes expressing 1N3R or 1N4R tau. **(l)** Histograms of the estimated calcium concentrations in the soma and processes of astrocytes. N=cultures/cells per culture. (**c**): LV-G1-CFP: 5/127, LV-G1-1N3R: 6/152, LV-G1-1N4R: 6/154 (**d-f**): LV-G1-CFP: 4/20, LV-G1-1N3R:4/19, LV-G1-1N4R:4/23. (**h,j,l**): LV-G1-CFP: 4/23, LV-G1-1N3R:4/21, LV-G1-1N4R:4/23. Data are presented as the mean ± SEM. One-sided ANOVA with Tukey's post-hoc test. Scale bars 20 µm (**b**) and 2 µm (**g,i,k**).

Figure 6: Impact of astrocytic tau overexpression on hippocampal function. (a-f) Immunofluorescence and confocal microscopy micrographs (left panels) and evaluations (right panels) of cell populations, 4 months after LV injection with LV-G1-GFP alone (white bars) and LV-G1-GFP + LV-G1-1N3R (yellow bars). (**a**) $DAPI^+$ cells (blue) in the hilus. **(b)** $NeuN^+$ neurons in the dentate gyrus. **(c)** PV^+ neurons (red) in the hilus. **(d)** $GluR2/3^+$ neurons in the hilus. **(e)** $BrdU^+$ cells in the subgranular zone of the dentate gyrus. **(f)** DCX^+ cells in the granule cell layer of the dentate gyrus. **(g)** Confocal micrograph (upper panel) and 3D reconstruction (lower panel) showing distal processes of astrocytes (green), in proximity of Gephyrin (blue) and VGAT (red) clusters. **(h)** Schematic representation (upper panels), 3D reconstructions (middle panels) and confocal micrographs (lower panels) of VGAT and Gephyrin clusters, unpaired (left panels) or paired (middle and right panels). **(i-l)** Quantification of VGAT and Gephyrin clusters in the territories of hilar astrocytes transduced with either a LV-G1-GFP (as control) or LV-G1-1N3R construct. (**i**) Density of $VGAT^+$ clusters. **(j)** Density of paired VGAT- Gephyrin clusters. **(k)** Density of Gephyrin clusters. **(l)** Gephyrin/VGAT cluster ratio. (**m**) Confocal micrographs and quantification of c-fos expression. **(n)** Schematics of the approximate position of the extracellular electrodes and local glutamate injection for oscillatory activity analysis. **(o)** Time-frequency plots of glutamate-induced gamma oscillatory activity (recordings with a peak frequency between 50 and 80 Hz) in the dentate gyrus. Right plot: statistical p-value for the difference between groups. **(p)** Power spectra (mean ± SEM) of glutamate-induced gamma oscillatory activity. **(q)** Power of gamma oscillations measured between 50 and 90 Hz. **(r)** Time-frequency plots of glutamate-induced fast oscillatory activity (recordings with a peak frequency between 90 and 110 Hz). Right plot: statistical p-value for the difference between groups. Time 0 corresponds to the onset of glutamate injection. **(s)** Power spectra of glutamate-induced fast oscillatory activity. **(t)** Power of fast oscillations measured between 80 and 120 Hz. (**a-f**): N=animals/sections per animal. LV-G1-CFP: 6/5, LV-G1-1N3R:6/5. (**i-l**): N=animals/cells per animal. LV-G1-CFP: 4/21, LV-G1-1N3R:4/24. (**m**): N=animals/sections per animal. LV-G1-CFP: 6/5, LV-G1-1N3R:6/5. (**i-l**): N=6 animals per group, 10 cells per animal. (**n-p**): N=6 animals per group and n=35-40 recordings. (**q-s**): N=6 animals per group and n=16-20 recordings. Data are presented as the mean ± SEM. Mann-Whitney two-tailed t-test (**a-f,i-l,q,t**) and one-sided ANOVA with two-tailed Tukey's post-hoc test (**p,s**). Scale bars: 20 µm (**a-f, m**), 5 µm (**g**), 250 nm (**h**).

Figure 7: Tau 3R overexpression in hilar astrocytes induces spatial memory deficit that is restored by NRG1p injection. (a) Schematic representation of the VSV-G pseudotyped LV and the experimental design used to evaluate the impact on cognitive function. Mice were injected with LV-G1-GFP alone or LV-G1-GFP + LV-G1-1N3R. **(b)** Schematic representation of the object location test. **(c)** Histogram showing the time spent interacting with the immobile and displaced objects. **(d)** Histogram of the percentage of time spent interacting with the displaced object. **(e)** Schematic representation of the learning task with Morris Water Maze and **(f)** histogram showing the latency to find the hidden platform. **(g)** Histogram showing the average number of crossings above the location of the target platform one day after spatial training. **(h)** Schematic representation of the learning reversal task. **(i)** Histogram of the latency to find the hidden platform. **(j)** Histogram of the percentage of time spent interacting with the displaced object of animals one hour after intraperitoneal injection of either a saline solution (sal., as control), or NRG1p. **(k)** Confocal micrographs of hippocampal slices showing DAPI (blue), PV^+ cells (red) and infected astrocytes (with LV-G1-GFP or LV-G1-GFP + LV-G1-1N3R) after intraperitoneal injections with saline solution or NRG1p. **(l)** Histogram of the density of PV^+ neurons in the hilus. (**m**) Confocal micrographs of PV^+ neurons in the hilus. DAPI (blue), PV (red) and infected astrocytes (green). (**n**) Histogram of the optical density of PV immunostaining in the hilus. N=animals. (j): LV-G1-CFP+sal: 8, LV-G1-1N3R+sal:7, LV-G1-1N3R+NRG1p:7. (**c-df-g,i**): LV-G1-CFP: 8, LV-G1-1N3R: 8. N=animals/cells per animal. (**l,n**): LV-G1-CFP+sal: 6/144, LV-G1-1N3R+sal :7/204, LV-G1-1N3R+sal: 4/68 Mann-Whitney two-tailed t-test (**c,d**), Wilcoxon signed-rank test to chance level with $^{###}p < 0.001$, $^{##}p < 0.05$, $^{#}p < 0.01$ (**d-j**), One-sided ANOVA with two-tailed Tukey's post-hoc test (**j,l,n**), two-sided ANOVA with two-tailed Dunnett's post-hoc test (**f,g,i**). Data are presented as the mean ± SEM. Scale bars: 25 µm (**k**) and 10 µm (**m**).

Materials and methods

Human patients.

The brains were collected with patients' informed consent and the authorization of the Ethics Commission of the Lausanne University Hospital and CHU of Lille. A total of 30 brains were examined, 21 sporadic AD cases without known familial history, and 9 control cases who showed no sign of neurological disorder and who were age-matched and sex-matched to patients (see **Supplementary Table 1 and Data Extended Fig. 1 a-c**). All AD cases have been hospitalized in the Service of Old Age Psychiatry of the Lausanne University hospital or CHU of Lille, and diagnosed according to the DSM-IIIR criteria. Clinical diagnosis and Braak stage were confirmed *post-mortem* by neuropathological examination in the department of Pathology of the Lausanne University Hospital for each case, following previously described protocols[61–63]. Tau phosphorylation was assessed using an antibody specific for the AT8 epitope in the anterior hippocampus, in the prefrontal, parietal, and temporal associative isocortex, and in the primary

717 visual cortex. The brains were removed with a *post-mortem* delay (PMD) of no more than 60 hours
718 and stored in buffered 10% formaldehyde until sampling.
719
720 **Immunohistochemistry on human samples**
721 Blocks of approximately 5 mm × 5 mm of the dorsal hippocampus, were embedded in paraffin and
722 cut into 20 µm-thick sections. To reduce autofluorescence, we followed a recently-developed
723 protocol[55,64]. Briefly, samples were incubated in a 0.5% sodium borohydride (NaBH4; Sigma-
724 Aldrich, 213462) solution, followed by a citrate buffer antigen retrieval (HC-AR) step. Then,
725 sections were microwaved for 10 min in tris buffer saline (TBS) and then incubated for 30 min in
726 95% formic acid (Sigma Chemical Co., St. Louis, MO). Slices were then rinsed and incubated 1h in
727 normal serum (rabbit or swine). Slices were then immersed for 48h at 4°C in the following primary
728 antibodies: (Mouse anti AT8, ThermoFisherMN1020, 1:500), (Mouse anti AD2, RAD 56484, 1:250),
729 (Mouse anti RD3, Merck 05-803, 1:75), (Mouse anti RD4, Merck 05-804, 1:150), (Rabbit anti
730 S100beta, ab41548, 1:500), (Mouse anti PSD95, ABR MA1-045, 1:75), (Mouse anti Amyloid Beta,
731 DAKO M0872, 1:100), (Mouse anti synaptophysin, ab8049, 1:250) for 24 h at 4°C. Supplemental
732 information is available in the Life Sciences Reporting Summary. Then, slices were rinsed and
733 incubated for 24h at 4°C in the following secondary antibodies: Alexa 488, 555, or 647 conjugated
734 highly cross-adsorbed donkey anti-goat, rabbit, mouse, rat or donkey anti mouse biotinylated.
735 Either the primary or the secondary antibody was omitted in negative-control sections. All sections
736 were counterstained for 10 min with DAPI (Merck; 1:5,000 dilution) to label nuclei.
737 Immunohistochemistry was followed by a final autofluorescence elimination step, using an
738 autofluorescence Eliminator reagent (EMD Millipore, 2160) and following the manufacturer's
739 instructions. Samples were mounted in VECTASHIELD Antifade Mounting Medium with DAPI
740 (VectorsLab, H-1200) and stored at 4°C until analysis.
741
742 **Quantification of human samples**
743 Quantification of $AD2^+$ cells, amyloid beta (Aβ) plaques, PSD95 and synaptophysin optical density
744 were performed on a minimum of 4 sections (separated by at least 160 µm) per patient, using a
745 digital camera (3CCD Hitachi HV-F202SCL) mounted on a slide scanner microscope (×20
746 objective, Zeiss axioscan Z1). AD2 inclusions were analyzed only when their surface was
747 comprised between 150 μm^2 and 2000 μm^2 and Aβ plaques between 350 μm^2 and 5000 μm^2. To
748 determine the presence of 3R and 4R tau inclusion in s100β-expressing astrocytes, we analyzed
749 15-20 stacks/patients, 40-60 $S100\beta^+$ astrocytes/patient and tau isoform, for a total of 1840
750 astrocytes for the presence of 3R tau and 1537 astrocytes for the presence of 4R tau.
751 The volume of $S100\beta^+$, 3R and 4R tau inclusions was determined using autoregressive algorithms
752 of the Imaris surface plugin[65]. Individual astrocytes were considered to contain 3R or 4R tau
753 inclusions when the volume of these inclusions represented at least 5 % of the volume of the
754 soma.

755

756 **Lentiviral vectors**

757 We used a new VSV-G pseudotyped LV to selectively express transgenes in astrocytes. The
758 gfaABC1D promoter was kindly provided by Dr. Michael Brenner[11,66] and ligated to the B(3)
759 enhancer to generate the G1 promoter, which was then cloned into the SIN-cPPT-gateway-
760 WPRE-miR124T transfer plasmids which contains four copies of the neuron-specific miRNA-124
761 target sequence (miR124T; full homology[67]) to repress transgene expression in neurons, the
762 woodchuck post-regulatory element (WPRE) and central polypurine tract (cPPT) to increase
763 transgene expression[68,69], and a 400-nucleotide deletion in the 3' long terminal repeat (self-
764 inactivating vector) to increase biosafety[70]. Human 1N3R and 1N4R tau isoforms with a V5 tag (14
765 aa, GKPIPNPLLGLDST inserted between the sequences encoding exons two and four)[36,71] and
766 the CFP reporter gene (Takara Bio Europe, France), were used to generate the SIN-cPPT-
767 GfaABC1D(B)3-tau-1N3R-V5 and SIN-cPPT-GfaABC1D(B)3-tau-1N4R-V5 (hereafter called LV-
768 G1-1N3R and LV-G1-1N4R), SIN-cPPT-GfaABC1D(B)3-GFP-WPRE-miR124T, and SIN-cPPT-
769 GfaABC1D(B)3-CFP-WPRE-miR124T (hereafter called LV-G1-GFP and LV-G1-CFP) plasmids.
770 MitoTimer was kindly provided by Prof. Terskikh[72]. The Mitochondrial ATP sensor was kindly
771 provided by H. Noji[20]. LV were produced as previously reported[73], using the packaging plasmid
772 pCMVΔ R8.92, the transfer vector expressing the transgenes, pRSV-Rev and pMD.2G (VSV-G
773 envelop). The final viral concentration was calculated by the p24 ELISA assay (RETROtek,
774 Kampenhout, Belgium).

775

776 **Primary rat hippocampal cultures**

777 For co-cultures, timed-pregnant rats (RjHan:WI, Janvier, Le Genest-St-Isle, France) were killed by
778 CO_2 inhalation and E17 embryos were collected in Petri dishes containing HBSS (Gibco, Life
779 Technologies, Zug, Switzerland), to enable hippocampal dissection. Cells were prepared following
780 published protocols[74]. The cells were plated at a density of 3 x 10^5 cells/cm^2 in neuronal medium in
781 multiwell dishes. For astrocyte cultures, P1 rat pups were used (Charles River, St-Germain
782 Nuelles, France) and cells were plated at a density of 20,000 cells/cm^2 in multiwell dishes.
783 Hippocampal co-cultures and primary hippocampal astrocytes were infected at DIV4 and DIV8
784 respectively, with 0.6 pg p24 antigen per cell of LV-G1-CFP, LV-G1-GFP, LV-G1-1N3R, LV-G1-
785 MitoTimer, or LV-G1-MitoGoAteam2, corresponding to 1.2 pg of p24 antigen for a double infection
786 and 1.8 ng for a triple infection.

787

788 **Dot blot procedure**

789 Increasing concentrations (0 to 500 ng in 200 µL PBS) of recombinant tau (3R or 4R) were loaded
790 onto nitrocellulose membrane (0.4 µm). Recombinant tau proteins were produced as described
791 previously[75], The membrane was incubated 1h at room temperature in a blocking solution

792 containing 5% milk-TNT (Tris 15 mM, NaCl 140 mM, Tween 20 0.05 %) and transferred to the
793 antibody solution diluted in 5% milk-TNT (mouse monoclonal antibody against 3R tau (RD3,
794 Millipore, 1/2000) or mouse monoclonal antibody against 4R tau (RD4, Millipore, 1/1000) for
795 incubation overnight at 4°C. Tau proteins were revealed by ECL chemi-luminescence (GE
796 Healthcare) using HRP-conjugated anti-mouse secondary antibody (Vector, 1/50 000). A negative
797 control without the primary antibodies was used to exclude non-specific signal.

798

799 **Protein extraction and immunoblotting**

800 Mouse hippocampus and cortex were dissected and suspended in PBS to a final concentration of
801 1 µg/µL. 10 µg were loaded onto a 4-12% Bis-Tris (Criterion gel, BIORAD), followed by transfer
802 onto a 0.45 µm nitrocellulose membrane. After 3 rinses, membranes were incubated with a
803 blocking solution for 30 min at room temperature before incubation with rabbit polyclonal anti-V5
804 (Millipore, AB3792, 1:10000) overnight at 4° C. The membrane was then incubated with the
805 secondary anti-rabbit HRP antibody for 45 min at room temperature (Vector: 1:5000). Signal was
806 visualized using ECL western blotting detection reagents (GE Healthcare) in an Amersham Imager
807 600.

808

809 **Animals and stereotaxic delivery of LV**

810 Three-month-old male C57Bl/6 mice were purchased from Janvier (Le Genest-St-Isle, France). All
811 animals were housed in a temperature-controlled room (22°C ± 1°C) and maintained on a normal
812 12-h light/dark cycle with access to food and water *ad libitum*. Mice were separated into cages of
813 four mice per cage. All procedures were performed in accordance with the overly strict Swiss
814 legislation on the care and use of laboratory animals. Mice were anesthetized by intraperitoneal
815 injection of a mixture of 100 mg/kg ketamine (Ketasol, Graeub, Bern, Switzerland) and 10 mg/kg
816 xylazine (Rompun, Bayer Health Care, Uznach, Switzerland). The animals received 2 µl of LV
817 bilaterally injected into the dorsal dentate gyrus at the coordinates: ±1.5mm lateral to the midline,
818 −2mm posterior to bregma, −2.4mm ventral to the dura relative to bregma. The LV were injected at
819 0.2 µl/ min and the needle was left in place for 5 min. Animals received injections of the analgesic
820 buprenorphine at a dose of 0.1 ml per 100 g post-injection.

821

822 **Immunohistochemistry on mouse samples**

823 For injected animals, mice were deeply anesthetized and transcardially perfused with 4%
824 paraformaldehyde. A series of 1-in-6, 30-µm thick coronal sections were prepared and incubated in
825 PBS containing 0.3% Triton-X100 with the following primary antibodies: (Chicken anti GFP,
826 Biotrend 55423, 1 :5000), (Rabbit anti CFP,Acris TA332666, 1 :250), (Rabbit anti GFAP (DAKO,
827 M0761, 1:500), (Mouse anti NeuN, Chemicon MAB377, 1:1000), (Mouse anti V5-Tag, Invitrogen

828 46-0705, 1:1000), (Goat anti V5-Tag , abcam ab9137, 1:1000), (GluR2/3, Millipore 07-598,
829 1:1000), (Mouse anti BrdU, CBL187, 1 :1000), (Rabbit anti anti VGAT, Synaptic Systems 131003,
830 1:1000), (Mouse anti Gephyrin, Synaptic Systems 131011, 1:500), (Rabbit anti Cfos,
831 Merck,ABE457, 1:500). Supplemental information is available in the Life Sciences Reporting
832 Summary. After several rinses with PBST, sections were incubated for 90 min at r.t. in a PBST
833 solution containing a mix of secondary antibodies: Alexa 488, 555, or 647 conjugated highly cross-
834 adsorbed donkey anti-goat, rabbit, mouse, rat, or guinea-pig (1:500; Life Technologies). All
835 sections were counterstained for 10 min with DAPI (Merck; 1:5,000 dilution) to label nuclei.
836 Immunohistochemistry against VGAT/Gephyrin was followed by a final autofluorescence
837 elimination step. To this end, Autofluorescence Eliminator reagent (EMD Millipore, 2160) was
838 used, as per the manufacturer's instructions. Samples were mounted in VECTASHIELD Antifade
839 Mounting Medium with DAPI (VectorsLab, H-1200) and stored at 4°C until analysis.
840
841 **Quantification of cell populations in the mouse hippocampus**
842 Quantification of DAPI$^+$, GFP$^+$, PV$^+$, GluR2/3$^+$, NeuN$^+$, V5$^+$, DCX$^+$, and BrdU$^+$ cells per brain was
843 performed from 1-in-6 sections spaced 300 µm apart using a digital camera (3CCD Hitachi HV-
844 F202SCL) on a slide scanner microscope (×20 objective, Zeiss axioscan Z1). In hippocampal
845 section containing infected cells, immunopositive cells located in the region of interest (molecular
846 layer; granular layer, subgranular layer, CA1, CA3, cortex and hilus) were counted using image
847 analysis software Zen 2 (black 8.0 edition and blue 2012 edition). Cell density was calculated by
848 dividing the total number of cells for each acquisition by the surface of each area of interest. For
849 PV labeling intensities, 100-150 cells were quantified in arbitrary units as the mean of all isolated
850 pixels of soma. Each OD was normalized via the subtraction of a slide-section in which signal was
851 absent (black). Normalization and recalibration across different experiments was achieved by using
852 internal control animals. Animal for the quantification of c-Fos$^+$ cells were perfused 90min after
853 memory test (object location task).
854
855 **Quantification and determination of cell phenotype *in vitro* and *in vivo***
856 Cell phenotypes were determined from 350 GFP$^+$ cells per mouse or 50 per neuron-glial culture.
857 Co-localization with GFAP, S100b, NeuN, or IBA1 were assessed by confocal microscopy (x40 oil
858 immersion objective, Zeiss LSM 710 Quasar) over the entire z-axis. Labeled cells were rotated in
859 orthogonal planes (x and y) to verify double labeling. All analyses were performed in sequential
860 scanning mode to prevent crossover between channels. The estimated fraction of GFP$^+$ cells co-
861 labelled with NeuN or GFAP was calculated for each animal. Absolute numbers of GFP$^+$/GFAP$^+$,
862 GFP$^+$/S100b$^+$, and GFP$^+$/NeuN$^+$ cells were obtained by multiplying the corresponding estimated
863 fraction of co-labelled GFP$^+$ cells by the total number of GFP$^+$ cells for each animal. GFP$^+$ cells
864 located in dentate gyrus were classified as astrocytes, RGL and neurons based on morphology.
865 Astrocytes were characterized by a large spheroid or pyramidal soma with ramified processes,

866 neurons displayed an oval-shaped soma with an apical dendritic tree extending through the
867 granular cell layer and reaching the molecular layer and RGL cells displayed a prototypical
868 morphology, including a nucleus located in the SGZ of the DG, a radial process extending through
869 the GCL and extensively branching into the outer GCL and the molecular layer and a few basal
870 processes extending towards the hilus [76,77].
871
872
873 **Morphological analyses of GFP+ astrocytes *in vitro* and *in vivo***
874 15-20 hilar GFP^+ astrocytes per mouse (or 50 GFP^+ astrocytes *in vitro*) were imaged with a Zeiss
875 LSM 880 Quasar confocal system (63x + 2x numerical zoom) equipped with Airyscan. Care was
876 taken to only image astrocytes with a soma entirely contained within the thickness of the section.
877 Images consisted of 50‑75 optical sections (z = 0.3 µm). Three-dimensional reconstructions of
878 series of confocal images were deconvolved (Huygens SVI) and analyzed using Imaris XT
879 (Bitplane AG) and "autopath" algorithm of the "filament" plugin. Soma volume was calculated using
880 the Imaris surface plugin[65] and was manually corrected to exclude the main processes. The
881 neuropil infiltration volumes (NIVs) were calculated as previously described[78]. Briefly, for every
882 astrocyte analyzed (20-25 cells per group), three randomly chosen regions of interest of 15µm x
883 15µm x 10µm, devoid of soma and large branches were imaged. Astrocytic processes were 3D
884 reconstructed in the hilus using Imaris software and their volume was measured.
885
886 **Quantification of Gephyrin and VGAT *punctae***
887 Images were acquired in the vicinity of distal processes of GFP^+ astrocytes that were entirely
888 contained within the section thickness. Typically, 40-50 images per group (around 10 per animals)
889 were acquired (series of 50‑75 multiple optical sections, z = 0.2 µm) with a Zeiss LSM 880 Quasar
890 confocal system (63x + 4x numerical zoom) equipped with Airyscan. Images were imported into
891 Imaris XT (Bitplane AG) and corrected for background. VGAT or Gephyrin dots were determined
892 using autoregressive algorithms of spot plugin. The density of VGAT and Gephyrin dots was
893 calculated by dividing the total number of dots for each acquisition by the volume of interest. For
894 the VGAT/Gephyrin pairing analysis, we used colocalized spot Matlab script with 0.3µm for the
895 closest distance between spot. The VGAT/Gepherin ratio was then calculated.
896
897 **MitoTimer mitochondrial analyses in the mouse hippocampus**
898 The hippocampal astrocytic mitochondrial system was assessed four months after co-infection with
899 LV-G1-CFP + LV-G1-MitoTimer or LV-G1-CFP + LV-G1-1N3R + LV-G1-MitoTimer. Multiple optical
900 sections (z = 0.3 µm) of confocal images were acquired throughout the section of cells located in
901 the polymorphic and subgranular layers of the dentate gyrus, with a Zeiss LSM 780 Quasar
902 confocal system (63x + 4x numerical zoom). Fluorescence images were captured using similar
903 mirror/filter, excitation, and detection parameters as those used for the *in vitro* experiments. For

904 localizing processes within mitochondria, acquisitions were imported into Imaris XT (Bitplane AG).
905 The green (500-540 nm) and red (580-640 nm) channels from MitoTimer were merged using the
906 Imaris channel arithmetic Matlab plugin to visualize whole mitochondria. Mitochondrial volume
907 reconstructions were performed using the Imaris surface plugin. To assess the redox state of the
908 mitochondria, the mean intensities of the red and green channels were automatically calculated
909 using the Imaris statistics plugin and normalized against those of the control condition (LV-G1-
910 CFP).
911
912 **Immunohistochemistry on primary cultures**
913 Primary cultures on glass coverslips were fixed and immunostained with the following primary
914 antibodies: chicken anti-GFP (Chemicon: AB16901, 1:500), rabbit anti-GFAP (Dako: Z0334,
915 1:1000), rabbit anti-NeuN (Chemicon: MAB377, 1:1000), mouse anti-V5 (Millipore AB3792, 1:500),
916 rabbit anti-CFP (Acris: TA332666, 1:250). Following washing, Alexa Fluor 594 goat anti-mouse
917 (Invitrogen, A11005) and Alexa Fluor 647 donkey anti-mouse (Mol. Probes A31571) were applied
918 (at a concentration of 1:500) for 30 min at r.t. Supplemental information is available in the Life
919 Sciences Reporting Summary. Coverslips were then imaged using a Leica SP5 confocal
920 microscope.
921
922 **MitoTimer mitochondrial system analyses *in vitro***
923 The astrocytic mitochondrial system was assessed 10 days after viral infection. Cells were imaged
924 by acquisition of multiple optical sections with a Zeiss LSM 710 Quasar confocal system.
925 **Morphology and localization:** Confocal images were imported into Imaris XT (Bitplane AG).
926 Green (500-540 nm) and red (580-640 nm) channels from MitoTimer were merged using the Imaris
927 channel arithmetic Matlab plugin to visualize whole mitochondria in CFP^+ cells and mitochondrial
928 volume reconstruction was performed using the Imaris surface plugin[65]. Using the CFP channel to
929 visualize the entire cell, a 20 µm diameter circle was drawn around the center of the soma of
930 astrocytes. Mitochondria found within this circle were considered as proximal and mitochondria
931 found further away were considered as distal. Mitochondrial distribution and morphology (length,
932 width, and surface) were automatically counted for each compartment and the frequency
933 distribution calculated in “proximal” and “distal” processes for each cell. **Motility:** For mitochondrial
934 motility, single mitochondria were manually followed for each time point from live imaging
935 acquisition based on merged green and red channels. The mean velocity and total track length
936 were then automatically calculated by Imaris. The total track length traveled (Δ) was used to
937 classify mitochondria as highly mobile (Δ ≥ 20 µm), mobile (6 µm ≤ Δ ≤ 20 µm), or stationary (6 µm
938 ≤ Δ). The direction of each mitochondria was determined by visualizing the displacement vector
939 and was defined as anterograde when the mitochondria moved towards the periphery of the
940 astrocyte and retrograde when it moved towards the soma. **MitoTimer redox state ratio**: The red
941 and green mean intensity were automatically calculated in the soma and proximal and distal

942 processes based on green and red merged channel volume reconstruction of MitoTimer using the
943 Imaris statistical plugin. The fluorescence ratio ($R^{555/488}$) was normalized against of the
944 fluorescence the control condition (LV-G1-CFP) for each culture.
945
946 **FRET mitochondrial ATP imaging**
947 The ATP mitochondrial system was assessed 10 days after viral infection. Astrocytes were
948 recorded every 5s for 5 min using a Zeiss LSM 710 Quasar confocal microscope with a 100X
949 objective and digital zoom set to 4. The excitation wavelength was 350 nm for CFP and 488 nm
950 for GFP, with detection of blue (410-480 nm), GFP (493-545 nm), and OFP (580–640 nm). The
951 OFP/GFP ratio was calculated by dividing the OFP mean intensity by the GFP intensity for 10
952 regions of interest in the soma and proximal and distal CFP^+ processes of astrocytes.
953
954 **Calcium imaging**
955 The intracellular calcium concentration was assessed 11 days after viral infection. Cultures were
956 loaded with 5 µM Fluo4 AM (Invitrogen) for 15 min in the presence of 0.02% pluronic F-127
957 (Invitrogen) at 37°C and 5% CO_2 in the dark in a HEPES-KRH buffer, pH 7.4 and de-esterified for
958 10–15 min before imaging. The mean fluorescence for Fluo4AM was normalized over CFP
959 fluorescence and calculated for 10 regions of interest in the soma and proximal and distal CFP^+
960 processes.
961
962 **In vitro electrophysiology**
963 **Slice preparation:** Mice (7 months old) were injected with viruses (LV-G1-1N3R, n=6) or CFP (LV-
964 G1-GFP, as controls, n=6) in the dentate gyrus and anesthetized with ketamine/xylazine, and
965 perfused with cold oxygenated sucrose-containing artificial cerebrospinal fluid (ACSF) (in mM: 252
966 sucrose,3 KCl,2 MgSO4, 1.2 CaCl2, 1.2 NaH2PO4, 24 NaHCO3, 10 glucose; pH 7.4) for 10 min
967 prior to decapitation. Three successive coronal brain slices (400 µm thick) containing both dorsal
968 hippocampi (Bregma about -1.5 to -2.7 mm) were prepared with a vibroslicer in cold sucrose-
969 containing ACSF, and placed in oxygenated recovery ACSF at 36°C for ~15 min. This recovery
970 solution was a NMDG/HEPES based ACSF (in mM: 93 NMDG, 20 HEPES, 2.5 KCl, 10 MgSO4,
971 0.5 CaCl2, 1.2 NaH2PO4, 30 NaHCO3, 3 sodium pyruvate, 2 thiourea, 5 ascorbic acid, 25
972 glucose; pH 7.3). Slices were then transferred into a "Haas" type interface chamber and
973 superfused with recording ACSF (in mM: 129 NaCl,3 KCl,1.8 MgCl2, 1.6 CaCl2, 1.25 NaH2PO4,
974 21 NaHCO3, 10 glucose; pH 7.4). After 1 hour, the ACSF temperature was slowly raised from
975 room temperature to 32 °C. **Recordings:** Field potentials were recorded with ACSF-filled glass
976 electrodes (~5 MOhm). Signals were amplified (differential amplification mode, gain 1000x, NPI
977 Ext-2 amplifiers), bandpass-filtered at 1-1000 Hz, and digitized at 2 KHz and acquired with Spike2
978 software (CED). In each hippocampal slice (6 per animal), electrodes were positioned at 4 different
979 sites in the granular layer / molecular layer interface of the dentate gyrus (**see Fig. 6n**). Transient

980 neuronal activity and high-frequency oscillations were evoked in the dentate gyrus by a short
981 pressure injection (200 ms, ~7-12 bars) of glutamate (10 mM in ACF) via a glass pipette (tip
982 diameter: ~8-12 µm) placed into the hilus (Pöschel et al. 2002). These experiments were
983 performed blindly without knowledge of the type of LV injected. After recording, slices were fixed
984 with 4% paraformaldehyde for latter verification by a second experimenter of the presence of GFP
985 labeled astrocytes in the dentate gyrus of the recorded slices. Only slices displaying proper LV
986 injection and expression in the dentate gyrus were used for further analyses (for LV-G1-1N3R: 5
987 mice and 22 hippocampal slices; for LV-G1-GFP: 5 mice and 19 hippocampal slices). **Analysis:**
988 Time-frequency decompositions were performed using the Matlab toolbox EEGLAB (version
989 14.1.1;(Delorme and Makeig, 2004) on recording segments comprising the 2 s before and the first
990 12 s following glutamate stimulation. Time-frequency decompositions (from 10 to 160 Hz, 1Hz
991 steps) were computed using Morlet waveform transforms (f0/σf = [3 0.5], 3-cycle wavelet with a
992 slow linear increase (coefficient 0.5)). Data were assessed for the normality using the Kolmogorov-
993 Smirnov and Shapiro-Wilk tests, and for the homogeneity of variance using the Levene test. When
994 the data did not meet the criteria of normality, they were first log transformed prior to the statistical
995 analyses. For each response type, the total power and the frequency at which the power was
996 maximal were compared between groups. Comparisons between groups were performed using
997 univariate ANOVAs. The Welch t-test was used however when the homogeneity of variance was
998 not met. The initial voltage deflection following local glutamate application and reflecting the overall
999 induced activity was used as covariate. Statistical analysis was performed with SPSS and
1000 significance was set to p=0.05.
1001
1002 **Behavioral procedures**

1003 Four months after viral injection, tests were performed in the following order: Group of animals
1004 were tested for Light-dark box (day 121), Y-maze (day 123), open-field (day 127), and object
1005 recognition or location (day 128) or for Morris water maze (days 120-128) and Contextual Fear
1006 conditioning (days 130-131). For NRG1p injections, another group of mice received one
1007 intraperitoneal injection of NRG1p (0.1 ug/kg in 0.9% saline; Prospec) or saline solution 1h before
1008 object location test and were sacrificed 90-100 min after test. **Dark/light box:** The dark/light box
1009 consisted of two compartments made with acrylic transparent glass, placed in the open-field arena,
1010 a black/dark compartment (40 cm × 20 cm × 15 cm- 2lux) and a white/illuminated compartment
1011 (same dimensions, 350 Lux). Both compartments were connected by an aperture. Each subject
1012 was released in the same corner of the illuminated compartment and the number of exits and total
1013 time in the lit compartment were recorded for 6 min. **Y-maze test:** This test was performed as
1014 previously described[79]. The symmetrical Y-maze, made of acrylic glass, consisted of three arms,
1015 each 40cm long, 15cm high, and 5cm wide. Each mouse was placed in the center of the Y-maze
1016 and was free to explore the arena for 6min. After each session, the maze was thoroughly cleaned
1017 using ethanol and water and dried. The number of entries was recorded for each mouse while

1018 observing the mouse via a camera; one entry was defined as both hind paws of the animal being
1019 completely inside the arm. The measure for working memory is the percentage of alternations, i.e.
1020 the number of triads divided by the maximum possible alternations (the total number of entries
1021 minus 2) x 100[80]. **Object location test:** This task is based on the spontaneous tendency of
1022 rodents previously exposed to two identical objects to preferentially explore the object that has
1023 been placed in a novel location, rather than the non-displaced object[81]. The day before the
1024 exploration phase, each mouse was placed in an open-field arena (35 cm × 34 cm × 40 cm-high,
1025 wall with a spatial pattern inside) for habituation and allowed to explore the arena for 10 min. The
1026 total distance travelled in the open-field was measured by video-tracking (Noldus Ethovision, The
1027 Nederland), to assess general motricity and activity. The next day, two identical objects were
1028 placed in the middle of the open-field arena and mice were allowed to explore them for 10 min. The
1029 time exploring the two objects was scored. Spatial memory was tested 24 h later when one of the
1030 objects (left or right counterbalanced) was moved to a new position. Mice were allowed to explore
1031 for 10 min. The time exploring the displaced object was calculated as the percentage of the total
1032 time exploring both objects. **Object recognition test:** This task is based on the spontaneous
1033 preference of rodents for novelty and their ability to remember previously encountered objects[82,83].
1034 The procedure, equipment, and analyses were similar to those described for the novel object
1035 location test, but the pattern inside the arena was removed. One day after habituation, two identical
1036 objects were placed in the middle of the open-field and the time the animal spent exploring each
1037 object was recorded. We ensured that every mouse spent the same amount of time exploring the
1038 objects and avoided any bias due to differences in individual levels of exploration by removing the
1039 animal once it had explored the objects for a cumulative total of 30 s. Animals that did not achieve
1040 this criterion within 10 min were excluded (2 animals in total). Recognition memory was tested 24 h
1041 after the exploration phase. Mice were reintroduced into the arena and exposed to two objects, a
1042 familiar object and a novel object, for which the positions of the two objects were identical to those
1043 of session 1. The familiar object was a triplicate copy of the sample used in session 1, to avoid
1044 olfactory trails. The mouse was allowed to explore for 10 min and the time spent exploring each
1045 object was recorded. The nature and position (left or right) of the new object was randomized. The
1046 open field was cleaned thoroughly between the introductions of each mouse to eliminate olfactory
1047 cues. Memory for the familiar object was evaluated by calculating the preference index for the
1048 novel object, expressed as the percentage of time spent exploring the novel object per total time
1049 spent exploring both objects. Independent groups of mice were used for the object location and
1050 object recognition tasks, so that each animal was submitted to either one or the other task. **Morris**
1051 **Water Maze**: During the training phase, mice were placed in a pool filled with opaque water set at
1052 25 °C. Training consisted of 6 days of 4 trials per day. The platform was always hidden in the
1053 South East quadrant of the pool but the mice were released at various points around the swimming
1054 pool, with the point of release being counterbalanced every day. The inter-trial interval was
1055 between 10 and 20 min. Swimming tracks were recorded using video hardware and Ethovision

software (Noldus, The Netherlands). Spatial memory was then assessed during a probe trial 24 h after the final training (Day 7). After establishing robust spatial preference for the platform location, either reversal trials were performed during which the platform was placed in a different location. At day 8, mice started a novel, 3 days training session (2 trials per day), where the platform was located in a new position (NW) to start reversal learning. Swim paths were recorded and analyzed by a tracking system (EthoVision, Noldus, The Netherlands). The assessed variables were escape latencies and, for the probe trials, times spent in target quadrants and platform place proximity indices (Gallagher et al., 1993). During the probe tests, time spent in each quadrant and the numbers of crossings over the location of the platform (virtual circle) compared to the mean crossing number of the three other virtual circles in the other 3 quadrants was calculated. **Contextual Fear Conditioning**: Mice were assessed for fear memory accuracy in a fear-conditioning paradigm. Training: Each mouse was introduced in a conditioning chamber (FCS-NG 46000, Ugo Basile, Italy) measuring 19x10x30 cm, with metal wire floor and transparent plastic wall, set in a white soundproof cubicle (context A). The floor of the chamber under the grid was lined with tissue paper, changed between mice. After 3 minutes, mice received a single, 2-s footshock (0.5 mA), and were removed from the chamber 15 s later. Conditioned freezing response to context A was assessed 24 h later, upon 3-minutes exposure to exactly the same chamber. The freezing time, defined as the absence of all movements with the exception of those related to respiration, was recorded by overhead cameras and measured using automated scoring systems (AnyMaze, Ugo Basile, Italy).

Sample sizes, calculations, and statistical analysis

Sample sizes are indicated in the legend of the corresponding figures. Human sample size was not predicted. We have used a collection of human samples composed of 9 healthy control individuals and 21 Alzheimer´s disease patients. For cellular and behavioral assays, the sample size was chosen to account for statistical variability of cultures (more than three cultures) and surgical and behavioral procedures (more than eight animals), based on previous studies[76,84]. Human samples were classified on the basis of neurological and neuropathological examination, in particular on the presence of tau and Aβ in the hilus. The order of culture and mouse used for infection, injection and behavioral procedures was randomized for each experiment. Investigators were blinded to group allocation when processing the tissue, performing cell counts, during confocal image acquisition and behavioral tests. The only reasons for exclusion were problems encountered during culture (such as culture contamination) or failure of the injection procedure (no fluorescence observed in the hippocampus). Values are presented as the mean ± SEM; N corresponds to the number of independent experiments and n to the overall number of values. Statistical analyses were performed on raw data with Graphpad Prism software v8.0. The normality of the data was verified using a Shapiro test. Data containing two experimental groups were analyzed using the

1093 Student's t-test (parametric observations), Mann-Whitney test (non-parametric observations), one-
1094 way and two-way ANOVA tests and Wilcoxon matched pairs test (non-parametric paired
1095 observations), followed by Tukey's post hoc analyses. Statistical analyses on data containing more
1096 than two experimental groups were performed using two-way ANOVA test, followed by Dunnett's
1097 post hoc analyses, to account for multiple comparisons.

1098 Data availability

1099 The data that support the findings of this study are available from the corresponding author upon
1100 request. The map sequence for LV construction and microscopy acquisition data have been
1101 deposited in Zenodo.org: 10.5281/zenodo.3953694

1102

1103 Methods only references

1104 61. Braak, H. & Braak, E. [Morphology of Alzheimer disease]. *Fortschr.Med.* (1990).

1105 62. Braak, H. & Braak, E. Staging of Alzheimer's disease-related neurofibrillary changes.
1106 *Neurobiol. Aging* (1995).

1107 63. Braak, H., Alafuzoff, I., Arzberger, T., Kretzschmar, H. & Tredici, K. Staging of Alzheimer
1108 disease-associated neurofibrillary pathology using paraffin sections and
1109 immunocytochemistry. *Acta Neuropathol.* (2006). doi:10.1007/s00401-006-0127-z

1110 64. Flor-García, M. *et al.* Unraveling human adult hippocampal neurogenesis. *Nat. Protoc.* **15**,
1111 668–693 (2020).

1112 65. Richetin, K. *et al.* Amplifying mitochondrial function rescues adult neurogenesis in a mouse
1113 model of Alzheimer's disease. *Neurobiol. Dis.* **102**, 113–124 (2017).

1114 66. De Leeuw, B. *et al.* Increased glia-specific transgene expression with glial fibrillary acidic
1115 protein promoters containing multiple enhancer elements. *J. Neurosci. Res.* **83**, 744–753
1116 (2006).

1117 67. Merienne, N. *et al.* Gene transfer engineering for astrocyte-specific silencing in the CNS.
1118 *Gene Ther.* 1–10 (2015). doi:10.1038/gt.2015.54

1119 68. Déglon, N. *et al.* Self-inactivating lentiviral vectors with enhanced transgene expression as
1120 potential gene transfer system in Parkinson's disease. *Hum. Gene Ther.* **11**, 179–190
1121 (2000).

1122 69. Sirven, A. *et al.* The human immunodeficiency virus type-1 central DNA flap is a crucial

1123 determinant for lentiviral vector nuclear import and gene transduction of human
1124 hematopoietic stem cells. *Blood* **96**, 4103–4110 (2000).

1125 70. Zufferey, R. *et al.* Self-inactivating lentivirus vector for safe and efficient in vivo gene
1126 delivery. *J. Virol.* **72**, 9873–80 (1998).

1127 71. Lobbestael, E. *et al.* Immunohistochemical detection of transgene expression in the brain
1128 using small epitope tags. *BMC Biotechnol* **10**, 16 (2010).

1129 72. Terskikh, A. *et al.* 'Fluorescent timer': protein that changes color with time. *Science* **290**,
1130 1585–1588 (2000).

1131 73. Hottinger, A. F., Azzouz, M., Déglon, N., Aebischer, P. & Zurn, A. D. Complete and long-
1132 term rescue of lesioned adult motoneurons by lentiviral-mediated expression of glial cell
1133 line-derived neurotrophic factor in the facial nucleus. *J. Neurosci.* **20**, 5587–93 (2000).

1134 74. Kaech, S. & Banker, G. Culturing hippocampal neurons. *Nat. Protoc.* **1**, 2406–2415 (2006).

1135 75. Qi, H. *et al.* Nuclear magnetic resonance spectroscopy characterization of interaction of Tau
1136 with DNA and its regulation by phosphorylation. *Biochemistry* **54**, 1525–33 (2015).

1137 76. Richetin, K., Petsophonsakul, P., Roybon, L., Guiard, B. P. B. P. & Rampon, C. Differential
1138 alteration of hippocampal function and plasticity in females and males of the APPxPS1
1139 mouse model of Alzheimer?s disease. *Neurobiol. Aging* **57**, (2017).

1140 77. Gebara, E. *et al.* Heterogeneity of Radial Glia-Like Cells in the Adult Hippocampus. *Stem*
1141 *Cells* **34**, 997–1010 (2016).

1142 78. Stogsdill, J. A. *et al.* Astrocytic neuroligins control astrocyte morphogenesis and
1143 synaptogenesis. *Nature* **551**, 192–197 (2017).

1144 79. Holcomb, L. A. *et al.* Behavioral changes in transgenic mice expressing both amyloid
1145 precursor protein and presenilin-1 mutations: lack of association with amyloid deposits.
1146 *Behav. Genet.* **29**, 177–85 (1999).

1147 80. Wall, P. & Messier, C. Infralimbic kappa opioid and muscarinic M1 receptor interactions in
1148 the concurrent modulation of anxiety and memory. *Psychopharmacology (Berl).* **160**, 233–
1149 244 (2002).

1150 81. Ennaceur, A., Neave, N. & Aggleton, J. P. Spontaneous object recognition and object
1151 location memory in rats: the effects of lesions in the cingulate cortices, the medial prefrontal
1152 cortex, the cingulum bundle and the fornix. *Exp. brain Res.* **113**, 509–19 (1997).

1153 82. Ennaceur, A. & Delacour, J. A new one-trial test for neurobiological studies of memory in
1154 rats. 1: Behavioral data. *Behav. Brain Res.* **31**, 47–59 (1988).

1155 83. Dodart, J. C., Mathis, C. & Ungerer, A. Scopolamine-induced deficits in a two-trial object
1156 recognition task in mice. *Neuroreport* **8**, 1173–8 (1997).

1157 84. Richetin, K. *et al.* Genetic manipulation of adult-born hippocampal neurons rescues memory
1158 in a mouse model of Alzheimer's disease. *Brain* **138**, 440–455 (2015).

1159

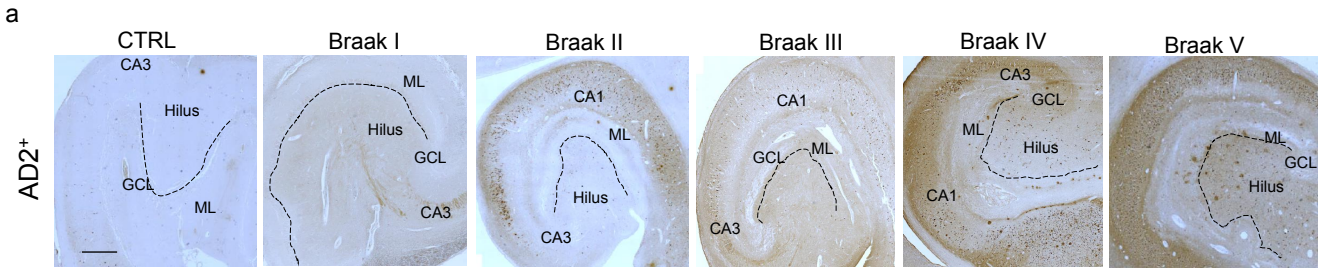

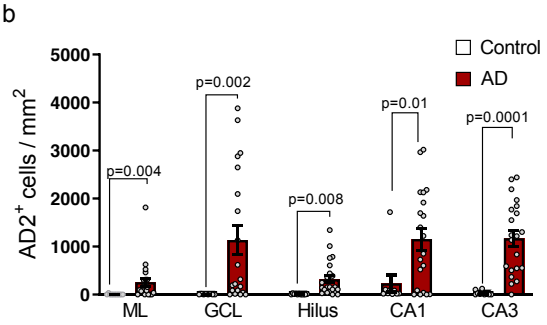

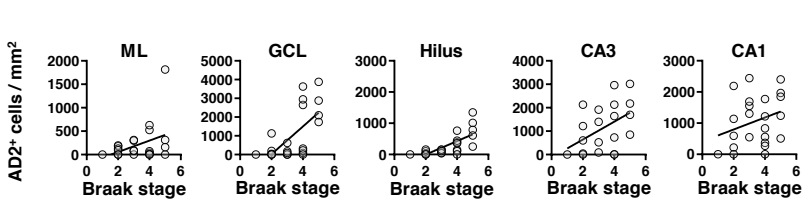

d

	Braak vs.ML	Braak vs.GCL	Braak vs.Hilus	Braak vs.CA3	Braak vs.CA1
R squared	0.1459	0.4313	0.5189	0.2571	0.1308
P value	0.0655	**0.0005**	**0.0001**	**0.019**	0.0824

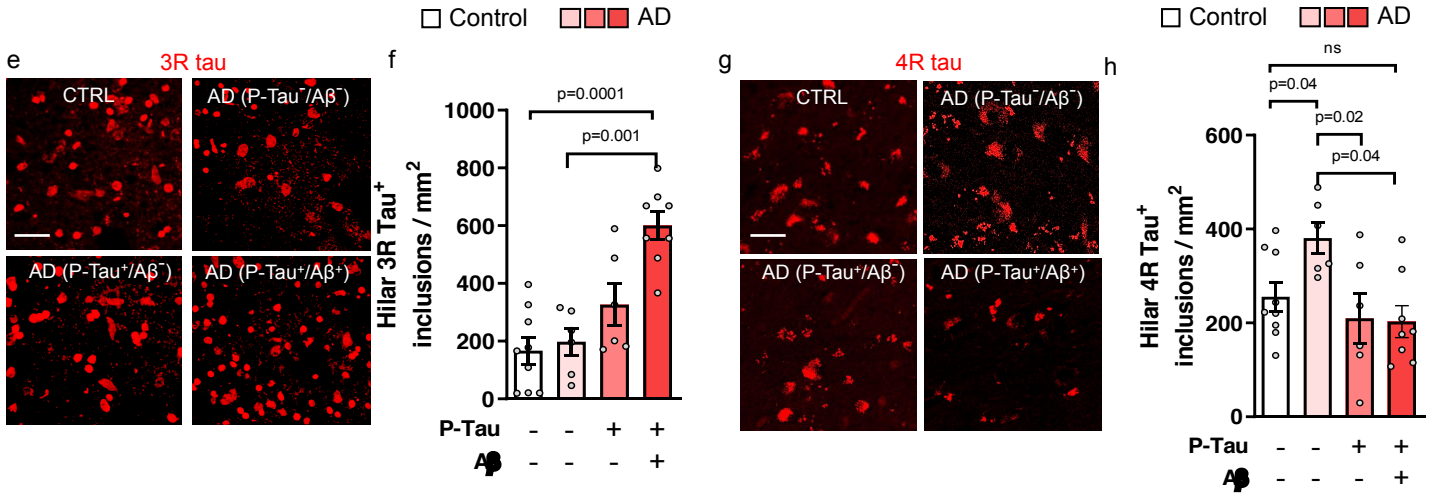

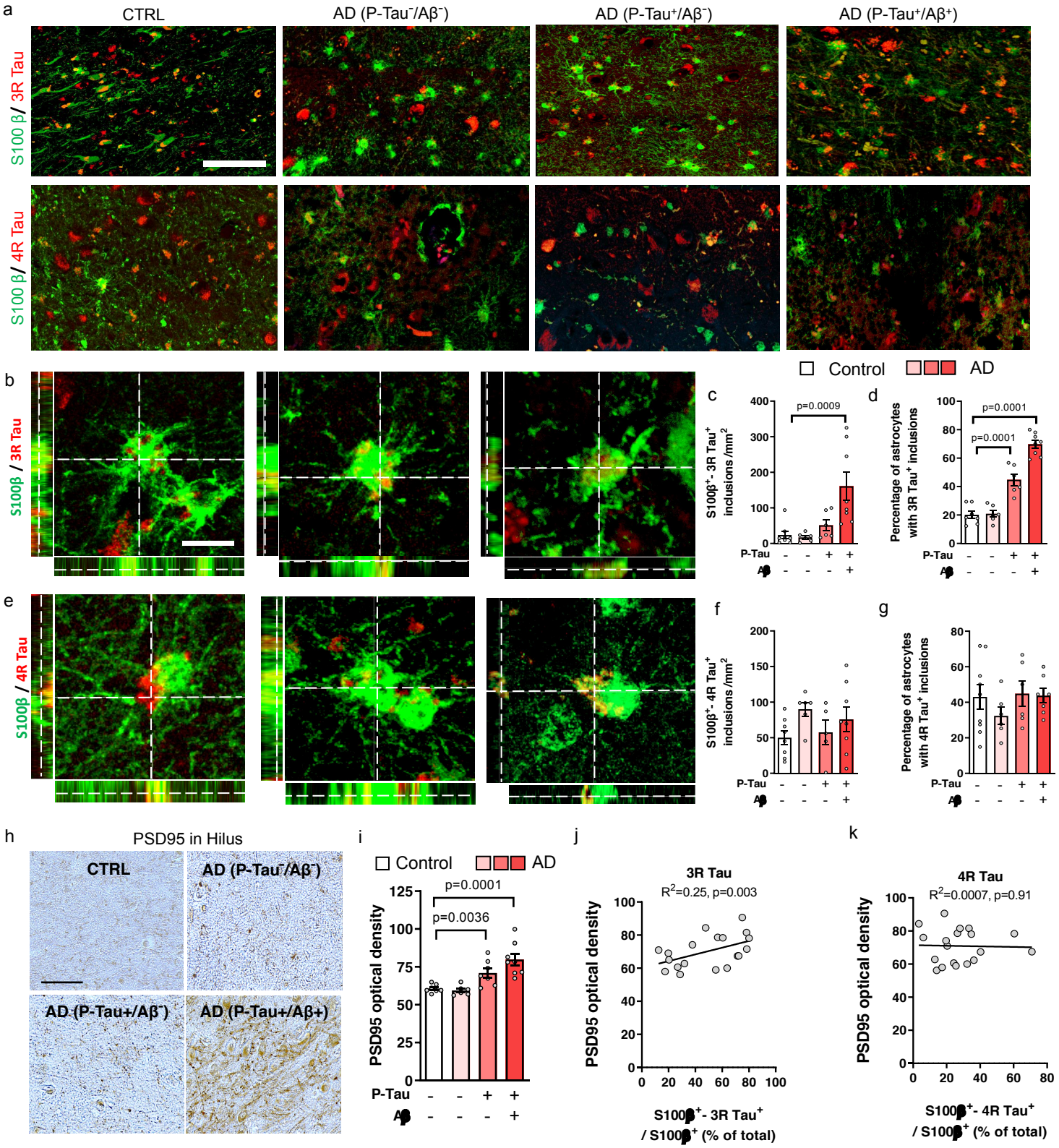
a
CTRL
AD (P-Tau⁻/Aβ⁻)
AD (P-Tau⁺/Aβ⁻)
AD (P-Tau⁺/Aβ⁺)
S100 β/ 3R Tau
S100 β/ 4R Tau
b
S100β / 3R Tau
Control
AD
c
S100β⁺- 3R Tau⁺ inclusions /mm²
p=0.0009
d
Percentage of astrocytes with 3R Tau⁺ inclusions
p=0.0001
p=0.0001
P-Tau
Aβ
e
S100β / 4R Tau
f
S100β⁺- 4R Tau⁺ inclusions /mm²
g
Percentage of astrocytes with 4R Tau⁺ inclusions
h
PSD95 in Hilus
CTRL
AD (P-Tau⁻/Aβ⁻)
AD (P-Tau+/Aβ⁻)
AD (P-Tau+/Aβ+)
i
Control
AD
PSD95 optical density
p=0.0001
p=0.0036
P-Tau
Aβ
j
3R Tau
R²=0.25, p=0.003
PSD95 optical density
S100β⁺- 3R Tau⁺ / S100β⁺ (% of total)
k
4R Tau
R²=0.0007, p=0.91
PSD95 optical density
S100β⁺- 4R Tau⁺ / S100β⁺ (% of total)

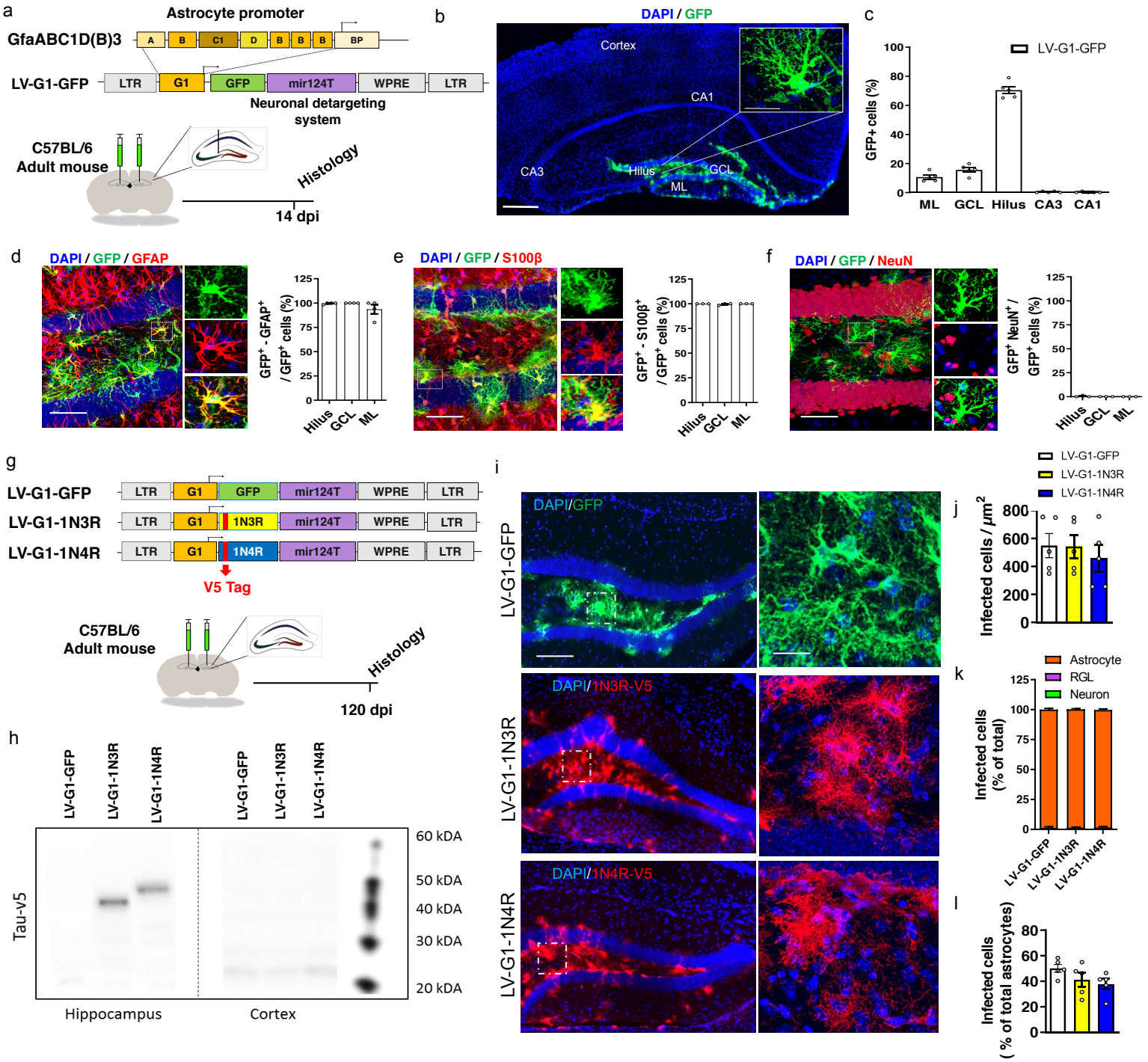
a
Astrocyte promoter
GfaABC1D(B)3
A
B
C1
D
B
B
B
BP
LV-G1-GFP
LTR
G1
GFP
mir124T
WPRE
LTR
Neuronal detargeting system
C57BL/6 Adult mouse
Histology
14 dpi
b
DAPI / GFP
Cortex
CA1
CA3
Hilus
GCL
ML
c
LV-G1-GFP
GFP+ cells (%)
ML
GCL
Hilus
CA3
CA1
d
DAPI / GFP / GFAP
GFP+ - GFAP+ / GFP+ cells (%)
Hilus
GCL
ML
e
DAPI / GFP / S100β
GFP+ - S100β+ / GFP+ cells (%)
Hilus
GCL
ML
f
DAPI / GFP / NeuN
GFP+ NeuN+ / GFP+ cells (%)
Hilus
GCL
ML
g
LV-G1-GFP
LV-G1-1N3R
LV-G1-1N4R
LTR
G1
GFP
1N3R
1N4R
mir124T
WPRE
LTR
V5 Tag
C57BL/6 Adult mouse
Histology
120 dpi
h
LV-G1-GFP
LV-G1-1N3R
LV-G1-1N4R
Tau-v5
60 kDA
50 kDA
40 kDA
30 kDA
20 kDA
Hippocampus
Cortex
i
LV-G1-GFP
DAPI/GFP
LV-G1-1N3R
DAPI/1N3R-V5
LV-G1-1N4R
DAPI/1N4R-V5
j
LV-G1-GFP
LV-G1-1N3R
LV-G1-1N4R
Infected cells / μm2
k
Astrocyte
RGL
Neuron
Infected cells (% of total)
LV-G1-GFP
LV-G1-1N3R
LV-G1-1N4R
l
Infected cells (% of total astrocytes)

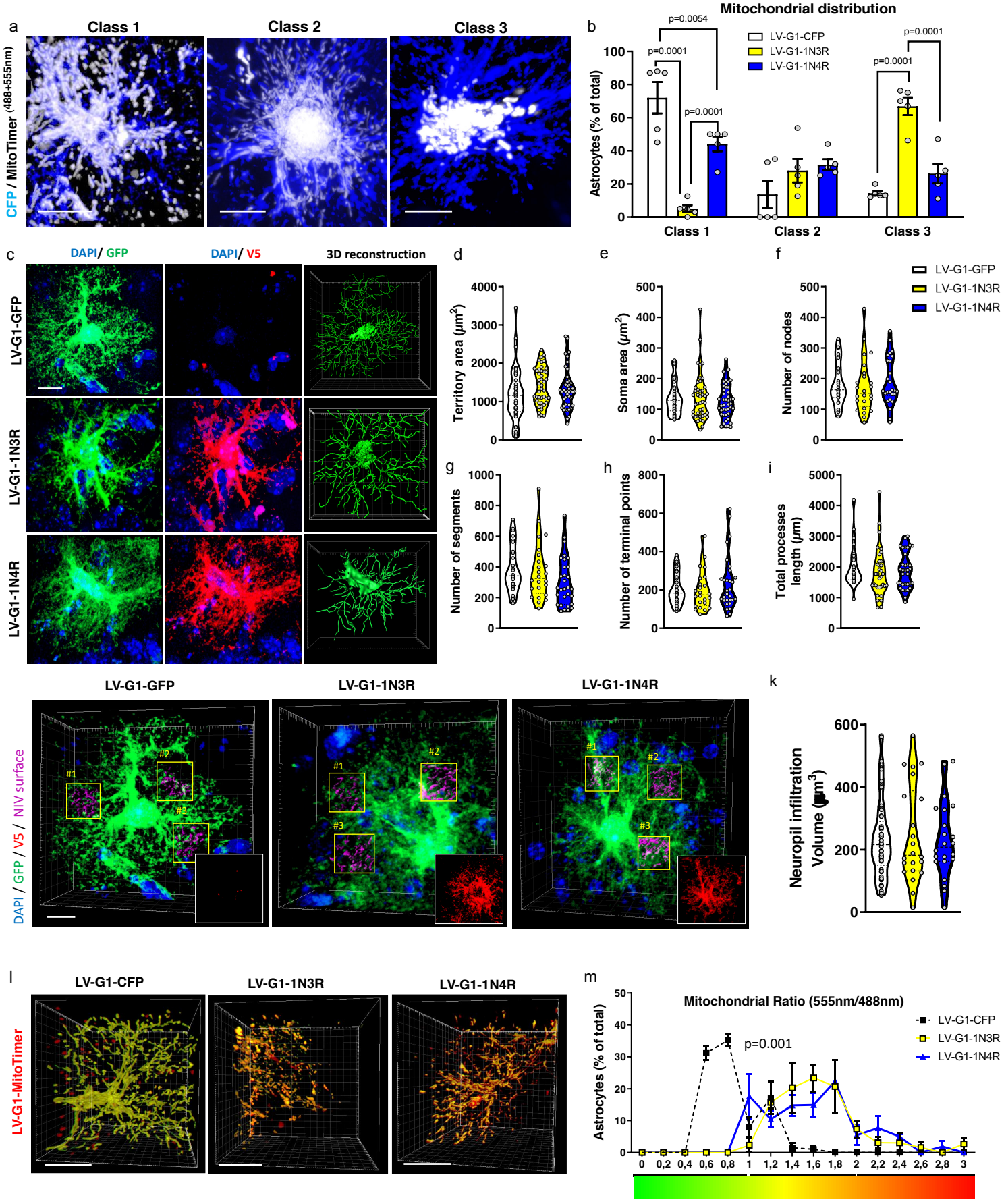
a
Class 1
Class 2
Class 3
CFP / MitoTimer (488+555nm)
b
Mitochondrial distribution
p=0.0054
p=0.0001
p=0.0001
p=0.0001
p=0.0001
LV-G1-CFP
LV-G1-1N3R
LV-G1-1N4R
Astrocytes (% of total)
Class 1
Class 2
Class 3
c
DAPI/ GFP
DAPI/ V5
3D reconstruction
LV-G1-GFP
LV-G1-1N3R
LV-G1-1N4R
d
Territory area (µm²)
e
Soma area (µm²)
f
Number of nodes
g
Number of segments
h
Number of terminal points
i
Total processes length (µm)
j
LV-G1-GFP
LV-G1-1N3R
LV-G1-1N4R
DAPI / GFP / V5 / NIV surface
#1
#2
#3
k
Neuropil infiltration Volume (µm³)
l
LV-G1-CFP
LV-G1-1N3R
LV-G1-1N4R
LV-G1-MitoTimer
m
Mitochondrial Ratio (555nm/488nm)
p=0.001
LV-G1-CFP
LV-G1-1N3R
LV-G1-1N4R
Astrocytes (% of total)

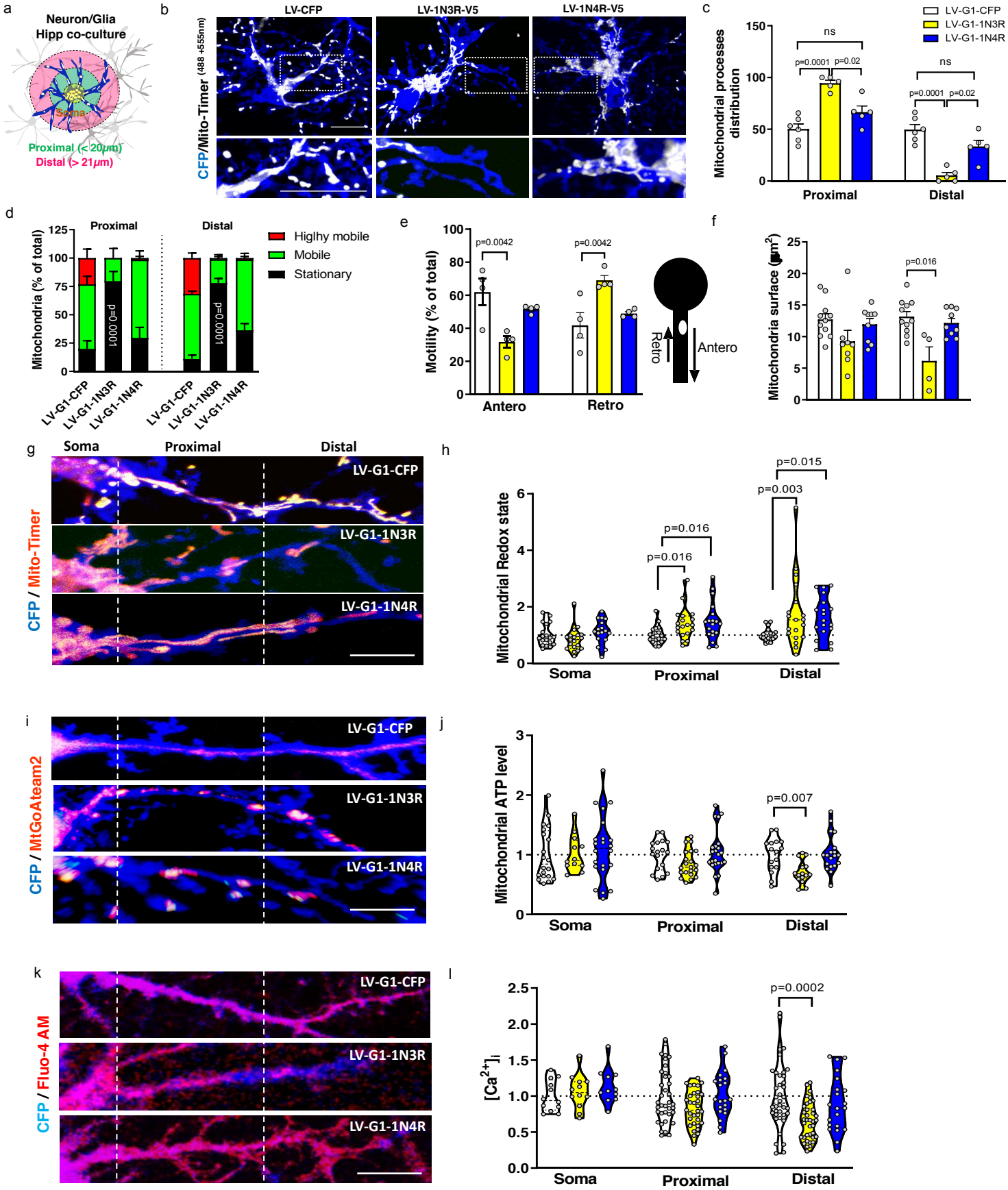
a
Neuron/Glia
Hipp co-culture
Soma
Proximal (< 20μm)
Distal (> 21μm)
b
LV-CFP
LV-1N3R-V5
LV-1N4R-V5
CFP/Mito-Timer (488 +555nm)
c
LV-G1-CFP
LV-G1-1N3R
LV-G1-1N4R
Mitochondrial processes distribution
ns
p=0.0001
p=0.02
Proximal
Distal
d
Proximal
Distal
Mitochondria (% of total)
Higlhy mobile
Mobile
Stationary
p=0.0001
LV-G1-CFP
LV-G1-1N3R
LV-G1-1N4R
e
Motility (% of total)
p=0.0042
Antero
Retro
f
Mitochondria surface (μm²)
p=0.016
g
Soma
Proximal
Distal
CFP / Mito-Timer
LV-G1-CFP
LV-G1-1N3R
LV-G1-1N4R
h
Mitochondrial Redox state
p=0.016
p=0.003
p=0.015
Soma
Proximal
Distal
i
CFP / MtGoAteam2
LV-G1-CFP
LV-G1-1N3R
LV-G1-1N4R
j
Mitochondrial ATP level
p=0.007
Soma
Proximal
Distal
k
CFP / Fluo-4 AM
LV-G1-CFP
LV-G1-1N3R
LV-G1-1N4R
l
[Ca2+]i
p=0.0002
Soma
Proximal
Distal

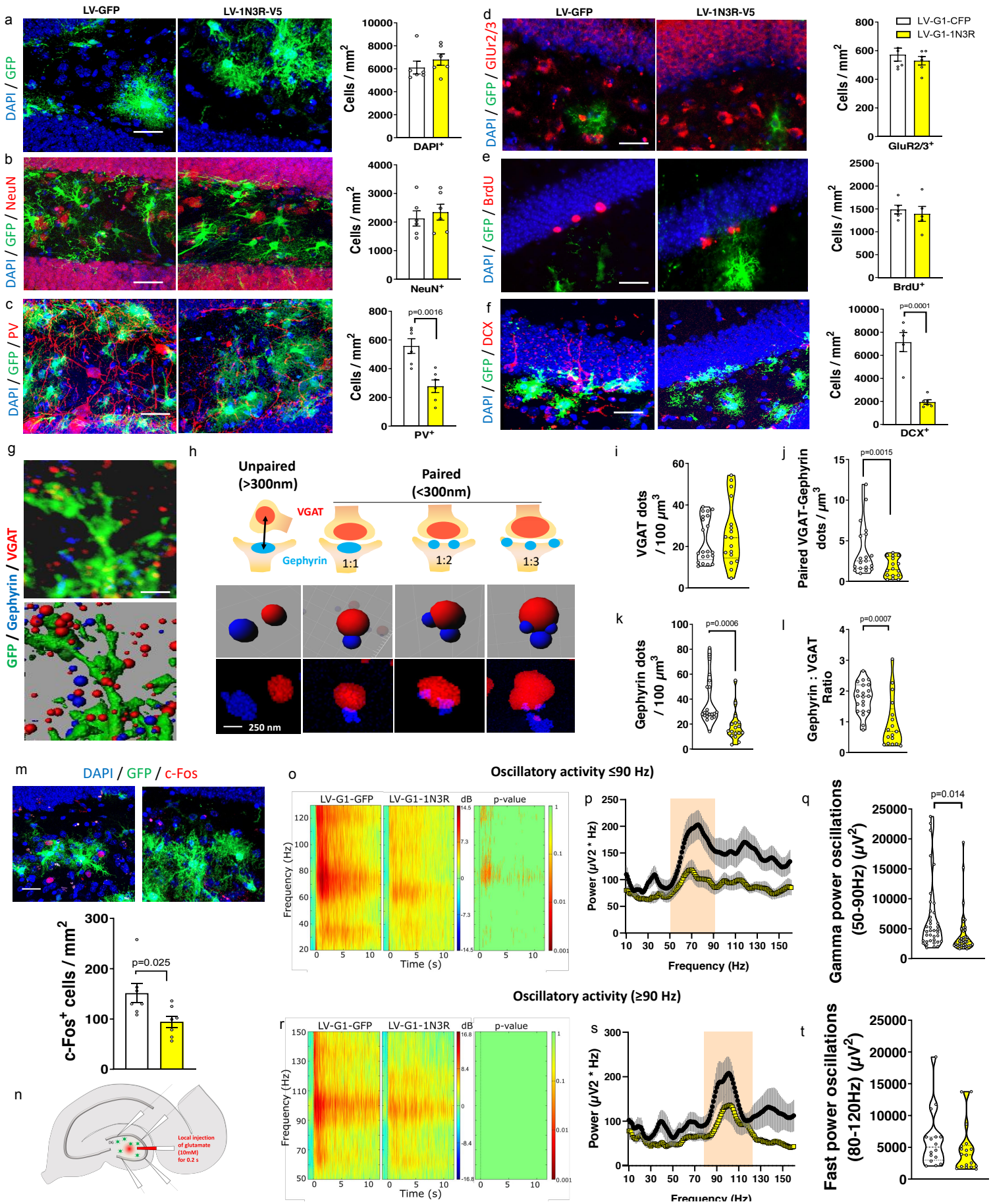
a
LV-GFP
LV-1N3R-V5
DAPI / GFP
Cells / mm2
DAPI+
b
DAPI / GFP / NeuN
NeuN+
c
DAPI / GFP / PV
p=0.0016
PV+
d
DAPI / GFP / GIUr2/3
LV-G1-CFP
LV-G1-1N3R
GluR2/3+
e
DAPI / GFP / BrdU
BrdU+
f
DAPI / GFP / DCX
p=0.0001
DCX+
g
GFP / Gephyrin / VGAT
h
Unpaired (>300nm)
Paired (<300nm)
VGAT
Gephyrin
1:1
1:2
1:3
250 nm
i
VGAT dots / 100 μm3
j
Paired VGAT-Gephyrin dots / μm3
p=0.0015
k
Gephyrin dots / 100 μm3
p=0.0006
l
Gephyrin : VGAT Ratio
p=0.0007
m
DAPI / GFP / c-Fos
c-Fos+ cells / mm2
p=0.025
n
Local injection of glutamate (10mM) for 0.2 s
o
Oscillatory activity ≤90 Hz)
LV-G1-GFP
LV-G1-1N3R
dB
p-value
Frequency (Hz)
Time (s)
p
Power (μV2 * Hz)
Frequency (Hz)
q
Gamma power oscillations (50-90Hz) (μV2)
p=0.014
Oscillatory activity (≥90 Hz)
r
s
t
Fast power oscillations (80-120Hz) (μV2)

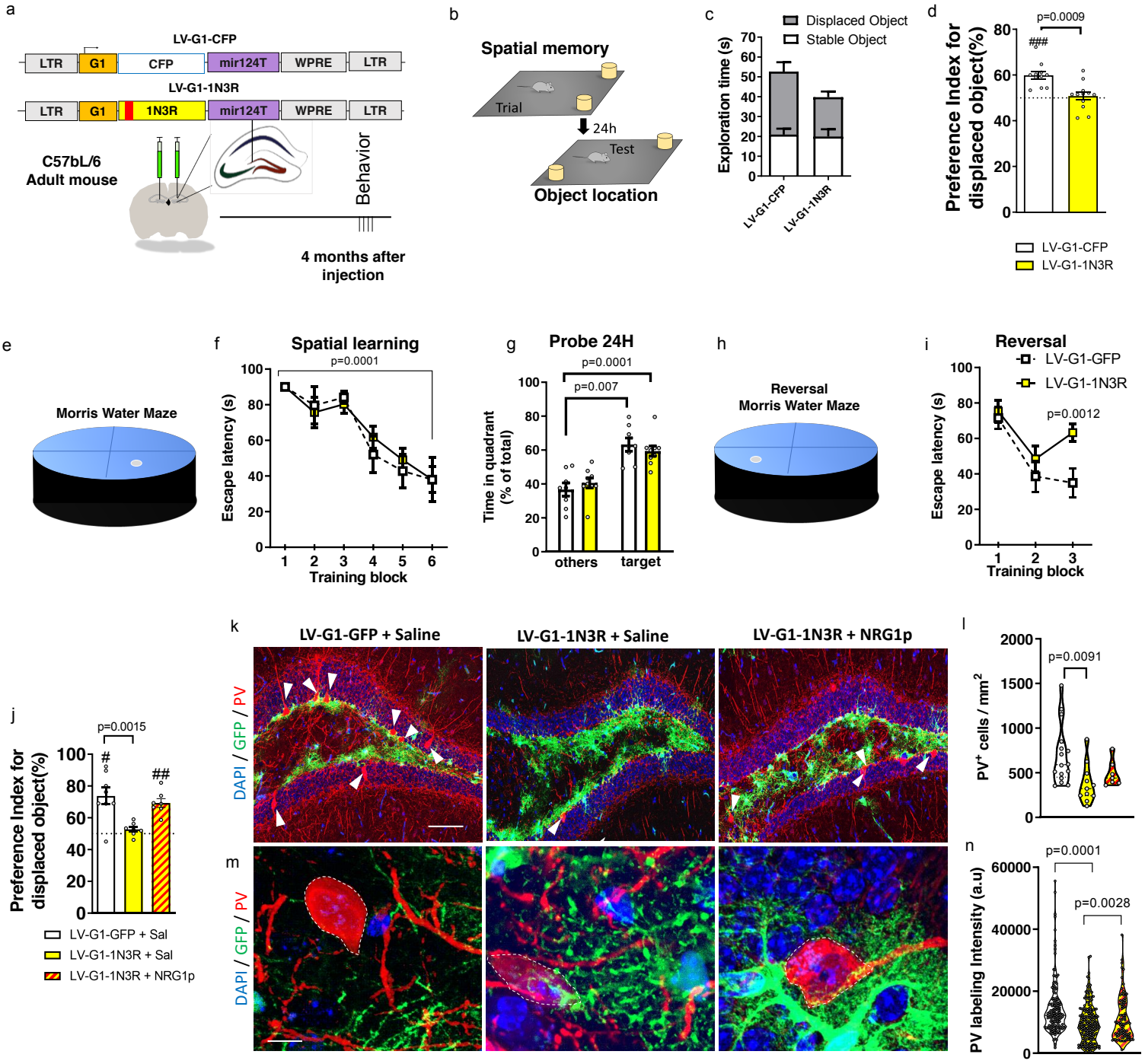
a
LV-G1-CFP
LTR
G1
CFP
mir124T
WPRE
LTR
LV-G1-1N3R
LTR
G1
1N3R
mir124T
WPRE
LTR
C57bL/6
Adult mouse
Behavior
4 months after injection
b
Spatial memory
Trial
24h
Test
Object location
c
Displaced Object
Stable Object
Exploration time (s)
LV-G1-CFP
LV-G1-1N3R
d
p=0.0009
###
Preference Index for displaced object(%)
LV-G1-CFP
LV-G1-1N3R
e
Morris Water Maze
f
Spatial learning
p=0.0001
Escape latency (s)
Training block
g
Probe 24H
p=0.0001
p=0.007
Time in quadrant (% of total)
others
target
h
Reversal
Morris Water Maze
i
Reversal
LV-G1-GFP
LV-G1-1N3R
p=0.0012
Escape latency (s)
Training block
j
p=0.0015
#
##
Preference Index for displaced object(%)
LV-G1-GFP + Sal
LV-G1-1N3R + Sal
LV-G1-1N3R + NRG1p
k
LV-G1-GFP + Saline
LV-G1-1N3R + Saline
LV-G1-1N3R + NRG1p
DAPI / GFP / PV
m
DAPI / GFP / PV
l
p=0.0091
PV+ cells / mm2
n
p=0.0001
p=0.0028
PV labeling Intensity (a.u)

Supplementary figures

Case	Group	Sex	Age (years)	PMD (h)	Cause of death	Braak stage	AD2^{+} in hilus	Aβ in Hilus
1	control case	M	71	48	cardiac failure	0	no	no
2	control case	F	71	22	retroperitoneal haemorhage	0	no	no
3	control case	F	75	26	cardiac failure	0	no	no
4	control case	F	77	48	pulmonary carcinoma	0	no	no
5	control case	F	89	24	renal carcinoma	0	no	no
6	control case	M	78	22	bladder carcinoma	0	no	no
7	control case	M	78	28	bronchopnemonia	0	no	no
8	control case	F	84	30	myocardial infarct	0	no	no
9	control case	M	71	48	cardiac failure	0	no	no
10	Alzheimer's Disease	F	87	30	Bronchopneumonia	3	no	no
11	Alzheimer's Disease	F	92	12	septic shock	2	no	no
12	Alzheimer's Disease	F	96	7	Bronchopneumonia	4	no	no
13	Alzheimer's Disease	F	101	37	renal haemorhage	3	no	no
14	Alzheimer's Disease	M	68	10	breathing failure	1	no	no
15	Alzheimer's Disease	M	58	5	septic shock	2	no	no
16	Alzheimer's Disease	M	89	7	Bronchopneumonia	4	yes	no
17	Alzheimer's Disease	F	90	24	digestive haemorrhage	5	yes	no
18	Alzheimer's Disease	F	80	26	pulmonary embolism	4	yes	no
19	Alzheimer's Disease	F	94	24	digestive haemorrhage	5	yes	no
20	Alzheimer's Disease	F	88	7	breathing failure	2	yes	no
21	Alzheimer's Disease	M	60	15	Undernutrition	1	yes	no
22	Alzheimer's Disease	F	65	6	Bronchopneumonia	5	yes	yes
23	Alzheimer's Disease	F	87	24	Bronchopneumonia	5	yes	yes
24	Alzheimer's Disease	F	80	21	renal insuffiency	3	yes	yes
25	Alzheimer's Disease	F	95	16	myocardial infarct	3	yes	yes
26	Alzheimer's Disease	M	84	31	Bronchopneumonia	5	yes	yes
27	Alzheimer's Disease	M	86	8	Bronchoaspiration	4	yes	yes
28	Alzheimer's Disease	M	84	20	Brochopneumonia	4	yes	yes
29	Alzheimer's Disease	M	92	20	heart failure	5	yes	yes
30	Alzheimer's Disease	M	88	18	NA	4	yes	yes

Supplementary Table 1: Patient data. Table with patient data. PMD: Post-mortem delay in hours.

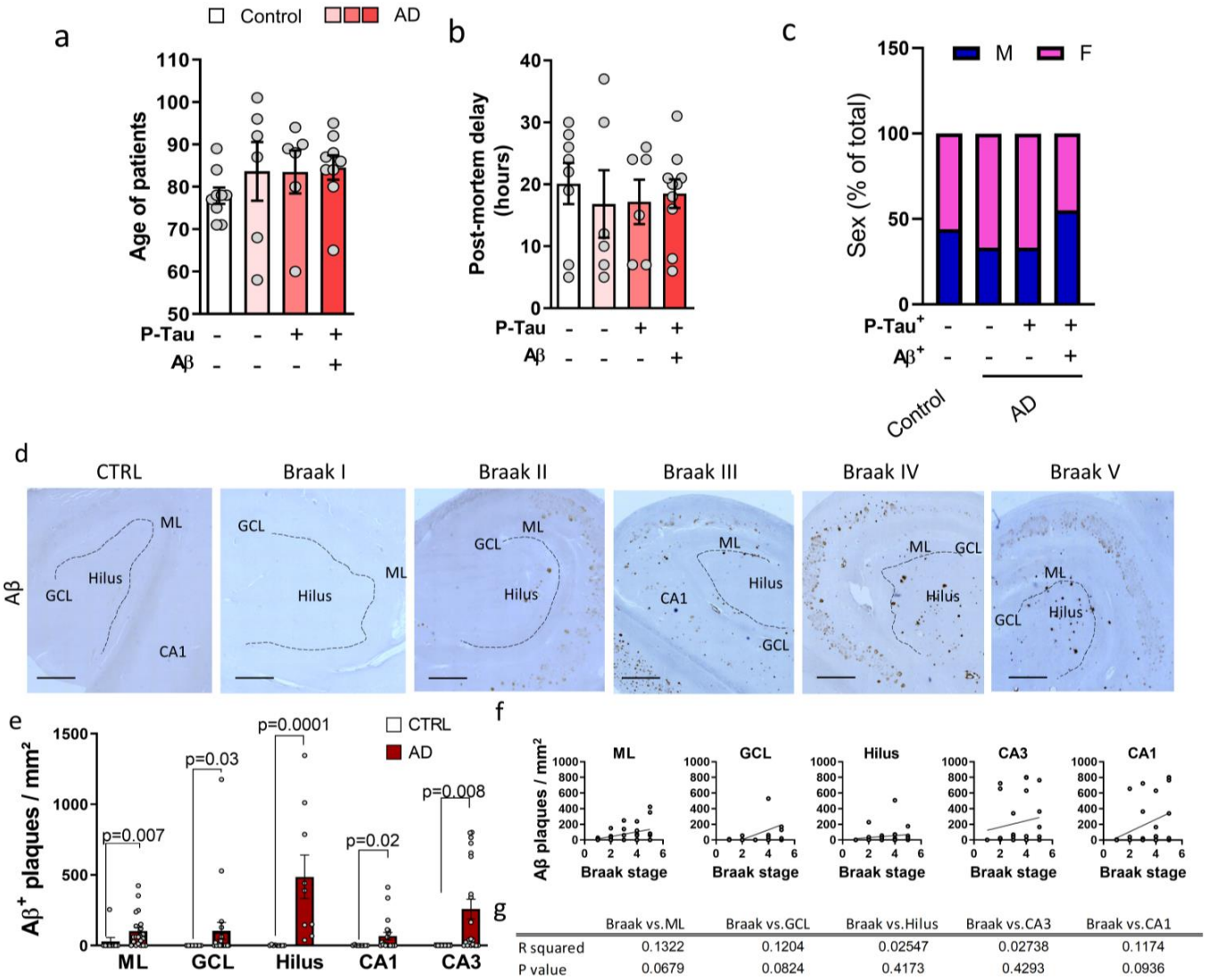

Supplementary Figure 1: Differential Aβ accumulation in the hilus of AD patients. (**a**) Histogram showing the age of patients. (**b**) Histogram showing the post-mortem delay of patients. (**c**) Histogram showing the sex of patients. **(d)** Photomicrographs of the human hippocampus showing the density of Aβ in healthy patient and AD donors. The different areas are indicated as black overlay. **(e)** Histogram showing the density of Aβ in the different hippocampal regions of healthy and AD donors. **(f)** Correlations between Aβ plaques density and Braak stage for patients, for each hippocampal area. **(g)** Table showing the correlation values and P values. Scale bars: 250 µm (**d**). N=patients/sections per patient; N=9/4 for Control, N=6/4 for AD (P-Tau$^-$/Aβ$^-$), N=6/4 for AD (P-Tau+/Aβ-), N=9/4 for AD (P-Tau+/Aβ+), (**a-c,e-g**). One-sided ANOVA with Tukey's post-hoc test (**a-c**), Mann-Whitney two-tailed t-test (**e**) and two-tailed Spearman's rank non-parametric correlation test (**g**). Data are presented as the mean ± SEM.

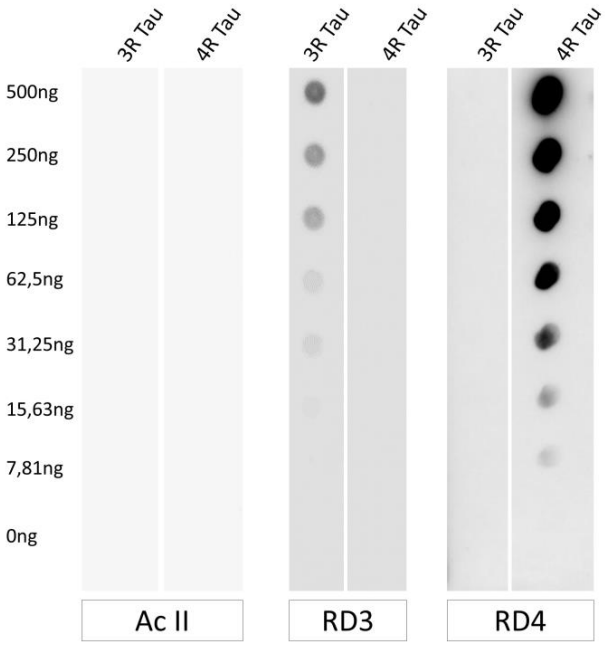

Supplementary Figure 2: RD3 and RD4 antibodies specificity. Dot-blot assay to test the specificity of the antibodies raised against 3R tau (RD3, middle panel), 4R tau (RD4, right panel) isoforms of tau or secondary antibody only (left panel).

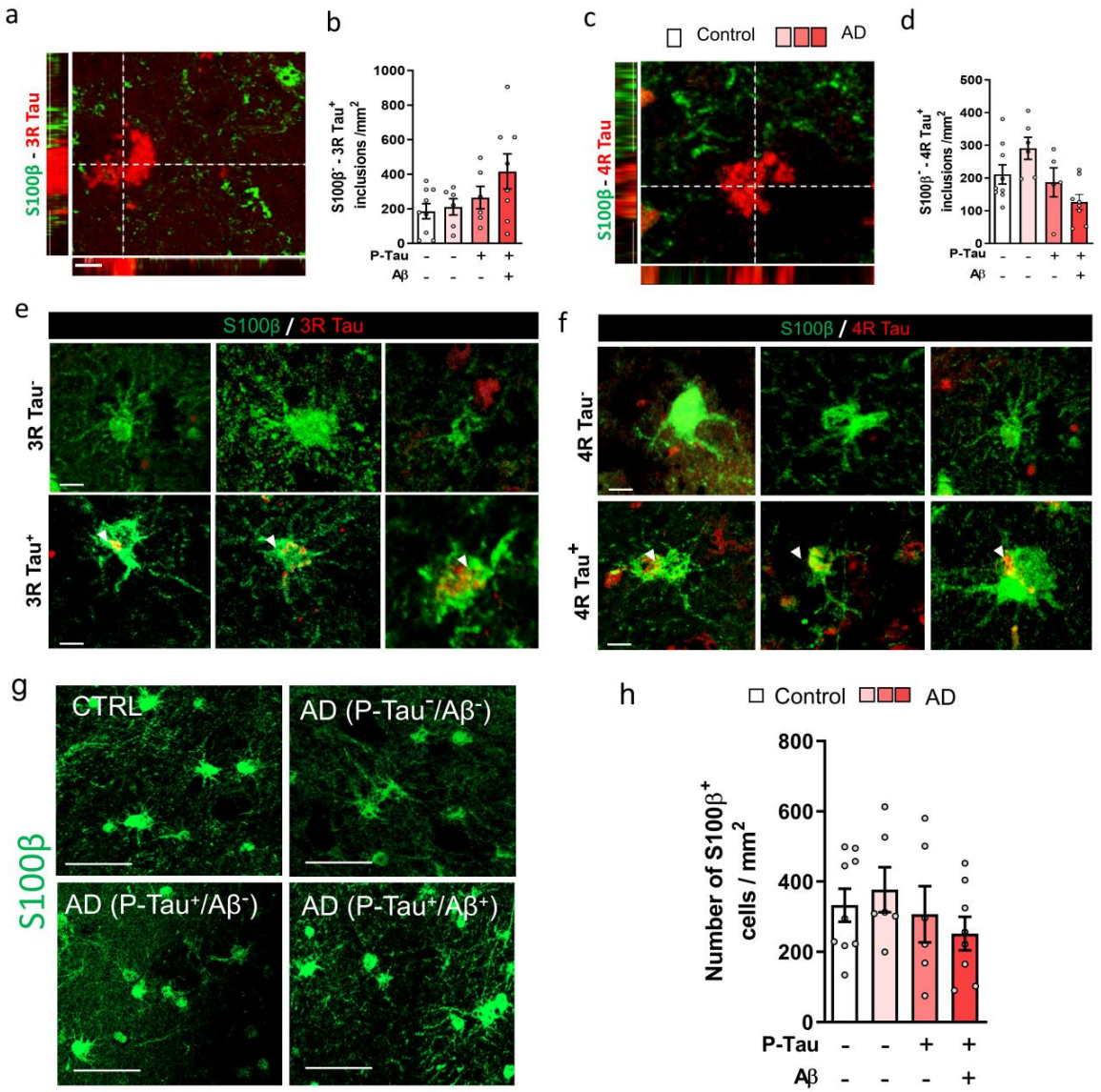

Supplementary Figure 3: Presence of tau isoforms in hilar cells. (a) Confocal micrograph of 3R tau inclusions (red) in a non-astrocytic (s100β⁻) cell. **(b)** Histogram showing the density of 3R tau inclusions in non-astrocytic cells of CTRL or AD patients. **(c)** Confocal micrograph of 4R tau inclusions (red) in a non-astrocytic cell. **(d)** Histogram showing the density of 4R tau inclusions in non-astrocytic cells. **(e)** Confocal micrographs showing hilar astrocytes (green) that do not contain 3R tau inclusions (red, top panels) or do contain tau 3R inclusions (bottom panels, white arrows). **(f)** Confocal micrographs showing hilar astrocytes (green) that do not contain 4R tau inclusions (red, top panels) or do contain tau 4R inclusions (bottom panels, white arrows). **(g)** Confocal micrographs showing S100β⁺ astrocytes (green) in the hilus of CTRL and AD donors. **(h)** Histogram showing the density of S100β⁺ astrocytes in the hilus of CTRL or AD patients. N=patients/sections per patient; N=9/4 for Control, N=6/4 for AD (P-Tau⁻/Aβ⁻), N=6/4 for AD (P-Tau+/Aβ-), N=8/4 for AD (P-Tau+/Aβ+), (**b,d,h**). One-sided ANOVA with Tukey's post-hoc test. Data are presented as the mean ± SEM. Scale bars: 10 µm (**a,c,e,f**) 50 µm (**g**).

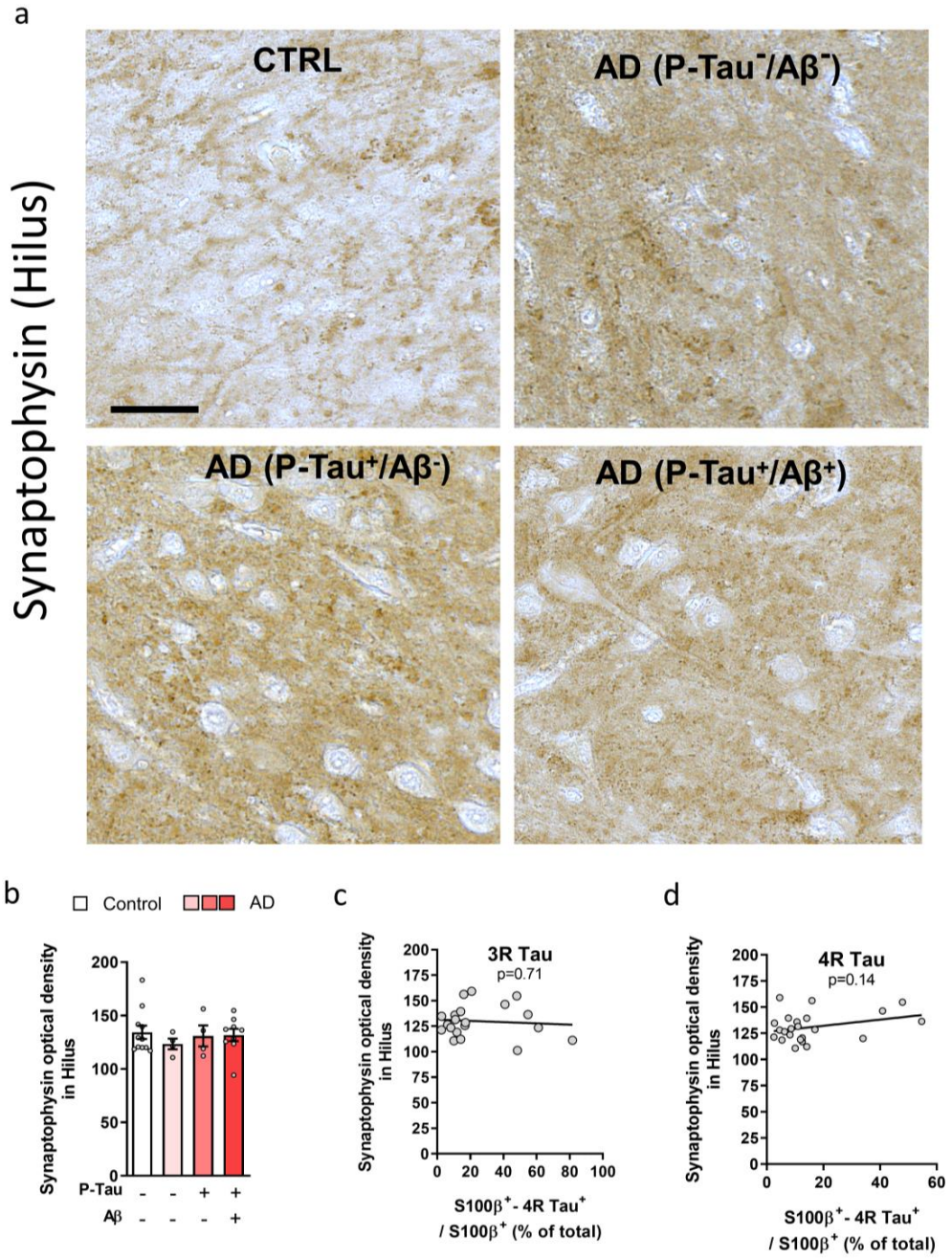

Supplementary Figure 4: Synaptophysin expression in the hilus of patients. (a) Photomicrographs showing Synaptophysin immunostaining in the hilus of CTRL or AD donors. **(b)** Histogram showing the intensity of Synaptophysin staining in CTRL or AD donors. **(c)** Correlation plot between the intensity of Synaptophysin staining and the number of hilar astrocytes expressing 3R tau in AD patients. **(d)** Correlation plot between the intensity of Synaptophysin staining and the number of hilar astrocytes expressing 4R tau in AD patients. N=patients/sections per patient; N=9/4 for Control, N=6/4 for AD (P-Tau⁻/Aβ⁻), N=6/4 for AD (P-Tau+/Aβ-), N=8/4 for AD (P-Tau+/Aβ+), (**b-d**). One-sided ANOVA with Tukey's post-hoc test (**b**) and two-tailed Spearman's rank non-parametric correlation test (**c-d**). Data are presented as the mean ± SEM. Scale bar: 25 µm.

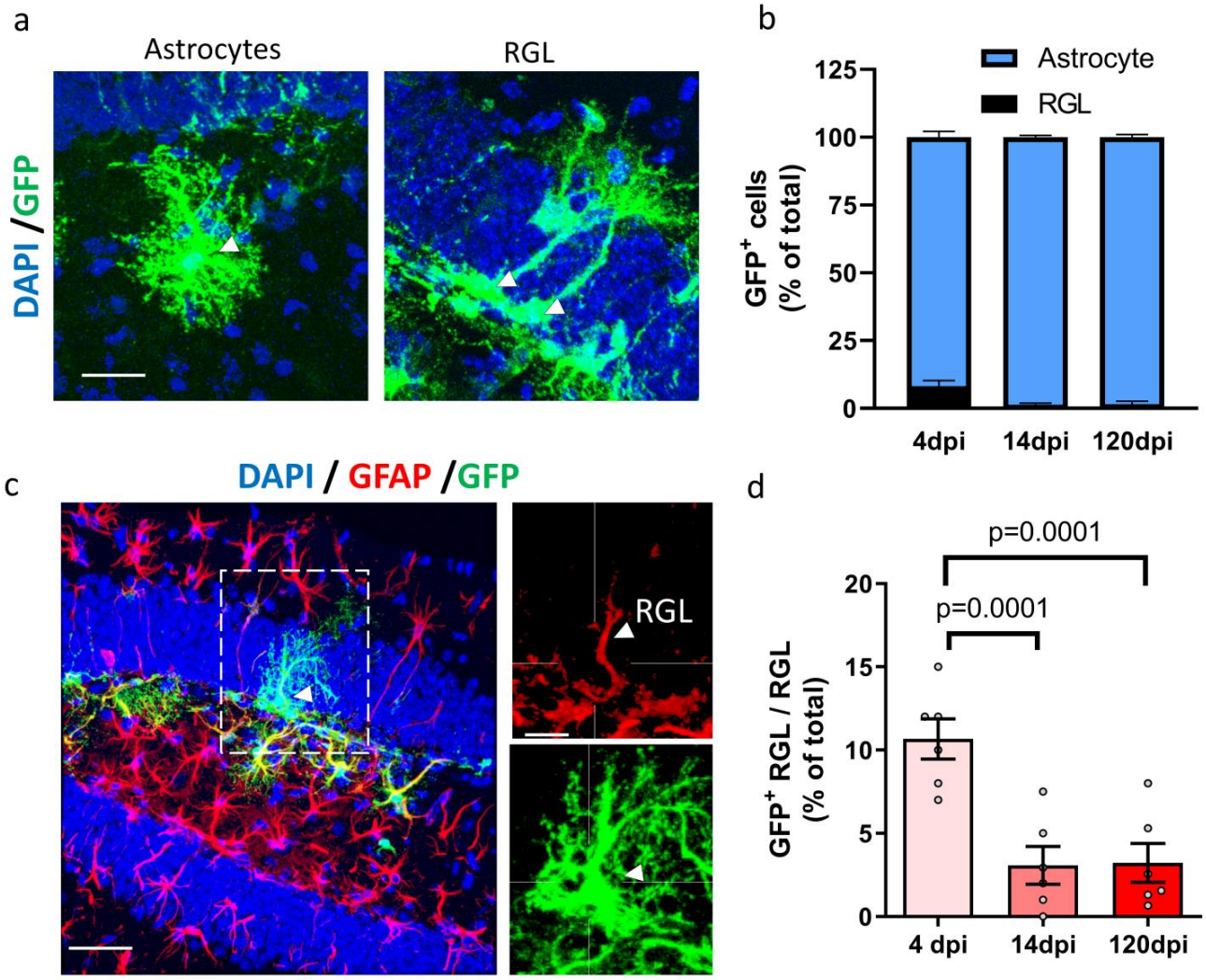

Supplementary Figure 5: LV-G1-GFP targets a small proportion of RGL stem cells of the dentate gyrus. **(a)** Confocal micrographs showing an astrocyte (left) and a Radial Glial-Like cell (RGL: right) that expressed GFP, 4 days after intrahippocampal injections of LV-G1-GFP. **(b)** Histogram showing the proportion of infected cells (GFP^+) that exhibited the morphology of astrocytes or RGL cells, 4, 14 and 120 days after intrahippocampal injections (dpi) of LV-G1-GFP. **(c)** Confocal micrographs showing a RGL cell expressing GFP and GFAP (red), 4 days after intrahippocampal injections of LV-G1-GFP. Right panels: One channel view of the cell shown on the left panel. **(d)** Histogram showing the proportion of RGL cells expressing GFP, 4, 14 and 120 days after intrahippocampal injections of LV-G1-GFP. N=animals/sections per animal; 4dpi: 6/5, 14dpi:6/5, 120dpi:6/5 (**b-d**). One-sided ANOVA with Tukey's post-hoc test (**d**). Data are presented as the mean ± SEM. Scale bars: 10 µm (**a**), 50 µm (**c**).

$

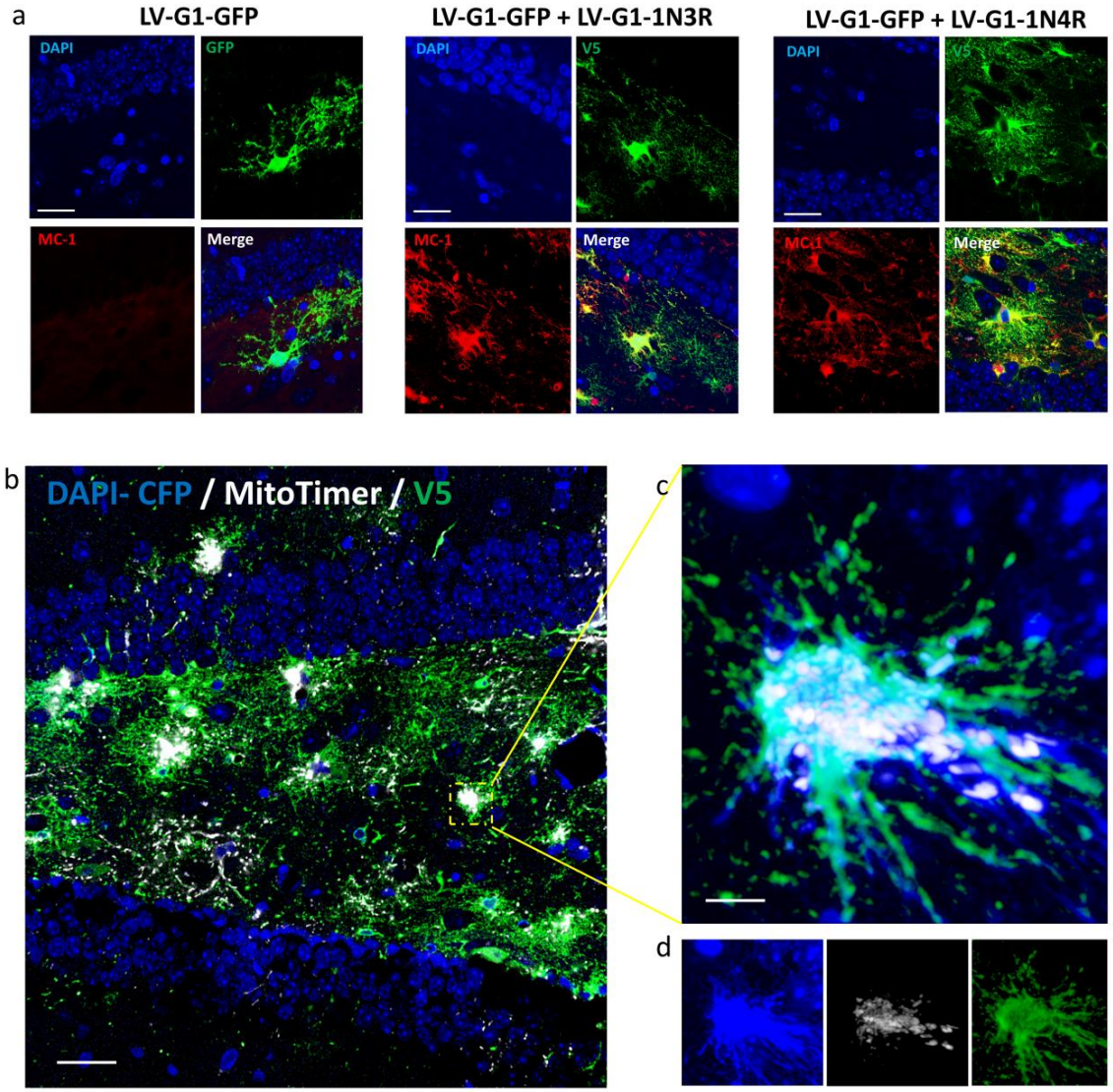

Supplementary Figure 6: Triple infection with LV-G1-CFP, LV-G1-1N3R and LV-G1-MitoTimer. (**a**) Confocal micrographs of the hilus, 120 days after intrahippocampal injections of LV-G1-GFP or LV-G1-1N3R + LV-G1-GFP or LV-G1-1N4R+ LV-G1-GFP showing the co-localization of GFP or V5 (green) and tau MC-1 (red). (**b**) Confocal micrograph showing the hilus of the dentate gyrus after infection with the 3 LVs. (**c**) Higher magnification view of the astrocyte highlighted on (**b**). (**d**) Three channel view of the same cell shown in (**b**). Scale bars: 10 µm (**a**), 25 µm (**b**), 5 µm (**c,d**).

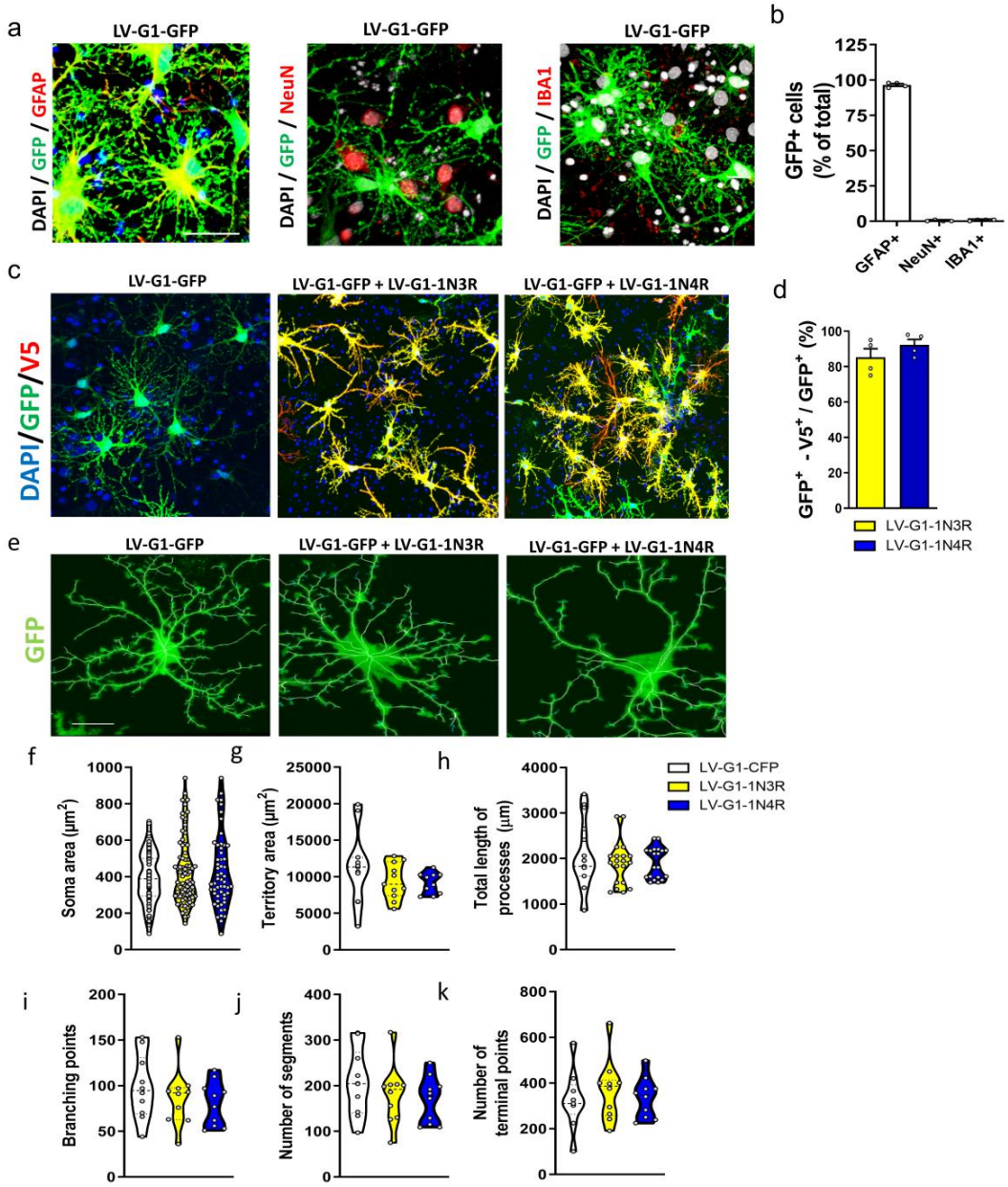

Supplementary Figure 7: In vitro targeting of astrocytes and morphological analyses. (**a**) Confocal micrographs of cultures infected with LV-G1-GFP showing the co-localization of GFP and GFAP (red, left panel), NeuN (red, middle panel) or Iba1 (red, right panel). (**b)** Histogram showing the proportion of infected cells that co-expressed GFP with GFAP, Iba1 or NeuN, (**c**) Confocal micrographs of cultures co-infected with LV-G1-GFP or LV-G1-1N3R + LV-G1-GFP or LV-G1-1N4R+ LV-G1-GFP. (**d**) Histogram showing the proportion of cells that were co-infected in the LV-G1-1N3R + LV-G1-GFP or LV-G1-1N4R+ LV-G1-GFP conditions. **(e)** Confocal micrographs of astrocytes after infection with LV-G1-GFP or LV-G1-1N3R+ LV-G1-GFP or LV-G1-1N4R+ LV-G1-GFP. Images are overlaid with a scaffold of the cell's morphology. (**f-k**) Violin graphs of the astrocytes' **(f)** soma area, (**g**) total territory area, (**h**) total length of processes, (**i**) number of branching points, (**j**) number of segments, (**k**) number of terminal points. N=cultures/cell per culture. (**b**): LV-G1-CFP: 4/203. (**d**): LV-G1-1N3R: 4/102 and LV-G1-1N3R: 4/97. **(f):** LV-G1-CFP: 4/70, LV-G1-1N3R: 4/81 and LV-G1-1N3R: 4/55. (**g-k**): LV-G1-CFP: 4/12, LV-G1-1N3R: 4/12 and LV-G1-1N3R: 4/12. Data are presented as the mean ± SEM. One-sided ANOVA with Tukey's post-hoc test (**b,f-k**) and Mann-Whitney two-tailed t-test (**d**). Data are presented as the mean ± SEM. Scale bars: 50 µm (**c**), 20 µm (**a,e**).

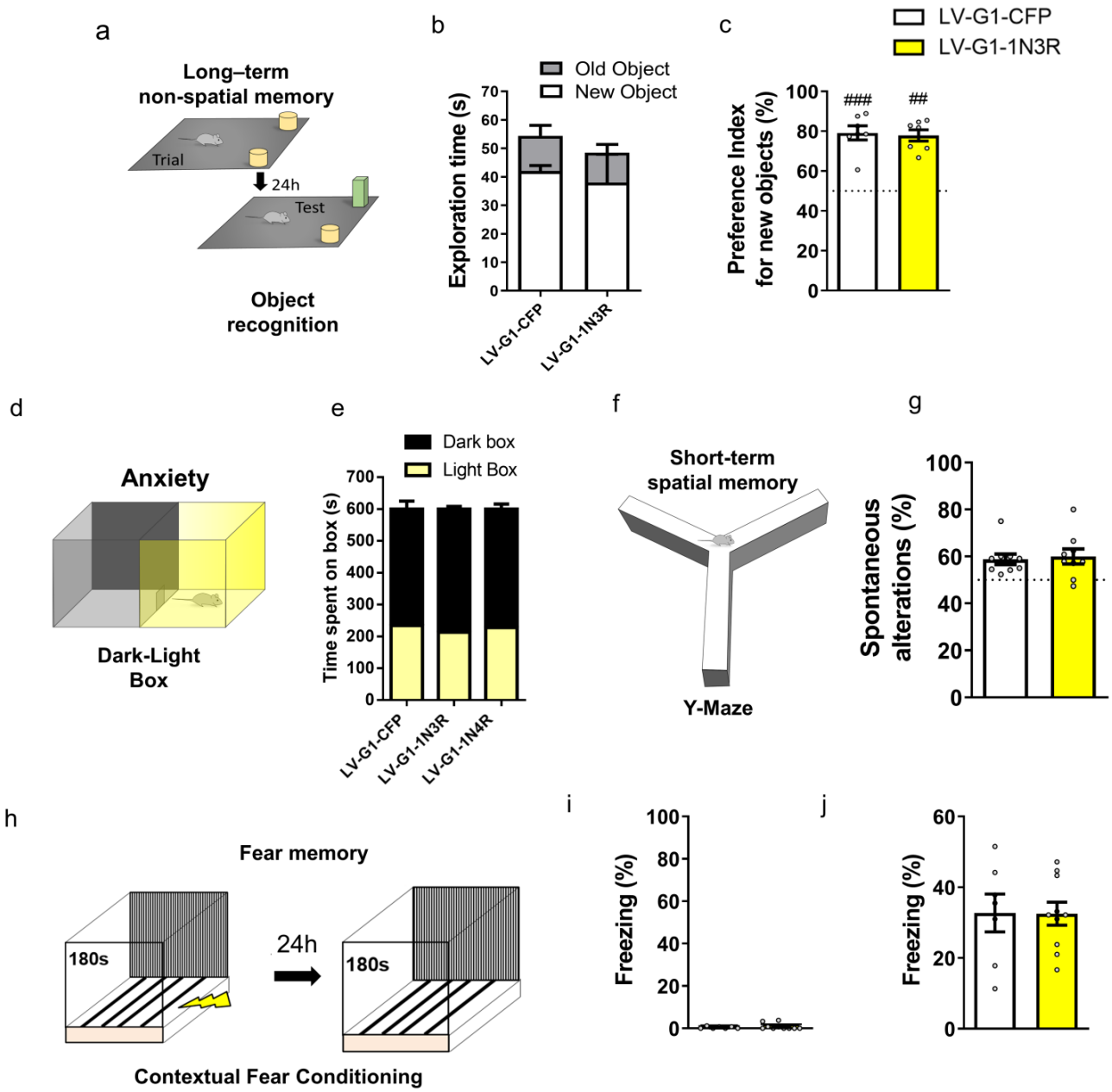

Supplementary Figure 8: 3R tau accumulation in hilar astrocytes does not impact behaviors that are not related to spatial memory. (a) Schematic representation of the object recognition task. **(b)** Histogram of the time spent interacting with the new and old object in animals infected with the LV-G1-GFP (white bars) or LV-G1-1N3R (yellow bars) LV. **(c)** Histogram of the percentage of time spent interacting with the new object. **(d)** Schematic representation of the dark/light box test. **(e)** Histogram showing the time spent in each compartment. **(f)** Schematic representation of the Y-maze. **(g)** Histogram of the spontaneous alterations between each arm. **(h)** Schematic representation of the contextual fear conditioning. **(i)** Histogram showing the percentage of freezing time before fear conditioning. **(j)** Histogram showing the percentage of freezing time 24H after fear conditioning. LV-G1-CFP, N=9 mice; LV-G1-1N3R, N=12 mice. Data are presented as the mean ± SEM. Mann-Whitney two-tailed t-test (**b,c,e,g,l,j**), Wilcoxon signed-rank test to chance level with $^{###}p < 0.001$, $^{##}p < 0.05$, $^{#}p < 0.01$ (c). Data are presented as the mean ± SEM.

Supplementary Video 1: Example of time-lapse confocal movie showing an astrocyte (left panel) in a neuron/glial hippocampal co-culture, infected with both LV-G1-CFP (to label the cell, in blue) and LV-G1-MitoTimer (to label mitochondria, in white). Right panel: higher magnification movie showing mitochondria dynamics in different regions of the astrocyte. Scale bar: 10 µm (left panel), 1 µm (right panel).

Supplementary Video 2: Example of time-lapse confocal movie showing an astrocyte in a neuron/glial hippocampal co-cultures, infected with either LV-G1-CFP and LV-G1-MitoTimer (left panel) or LV-G1-CFP, LV-G1-1N3R and LV-G1-MitoTimer (right panel). Scale bar: 10 µm.